NAVAL AIR WARFARE CENTER AIRCRAFT DIVISION
PATUXENT RIVER, MARYLAND

TECHNICAL REPORT

REPORT NO: NAWCADPAX/TR-2008/9

ANALYSIS AND TESTING OF FLEET CORRODED F/A-18C/D ARRESTMENT SHANKS

by

Mr. David T. Rusk, P.E.
Ms. Jennifer Pierce, UDRI
Mr. Wally Hoppe, UDRI
Mr. Brent Lancaster, ESRD, Inc.
Dr. Ricardo Actis, ESRD, Inc.
Dr. Barna Szabo, ESRD, Inc.

20 June 2008

DEPARTMENT OF THE NAVY
NAVAL AIR WARFARE CENTER AIRCRAFT DIVISION
PATUXENT RIVER, MARYLAND

NAWCADPAX/TR-2008/9
20 June 2008

ANALYSIS AND TESTING OF FLEET CORRODED F/A-18C/D ARRESTMENT SHANKS

by

Mr. David T. Rusk, P.E.
Ms. Jennifer Pierce, UDRI
Mr. Wally Hoppe, UDRI
Mr. Brent Lancaster, ESRD, Inc.
Dr. Ricardo Actis, ESRD, Inc.
Dr. Barna Szabo, ESRD, Inc.

RELEASED BY:

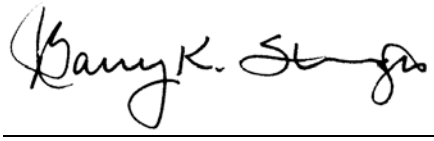

20 Jun 2008
BARRY STURGIS / CODE 4.3.3 / DATE
Head, Structures Division
Naval Air Warfare Center Aircraft Division

REPORT DOCUMENTATION PAGE

Form Approved
OMB No. 0704-0188

1. REPORT DATE	2. REPORT TYPE	3. DATES COVERED
20 June 2008	Technical Report	1 October 2003 – 30 September 2007

4. TITLE AND SUBTITLE

Analysis and Testing of Fleet Corroded F/A-18C/D Arrestment Shanks

5a. CONTRACT NUMBER
F42600-00-D-0039, 0011

5b. GRANT NUMBER

5c. PROGRAM ELEMENT NUMBER

6. AUTHOR(S)

Mr. David T. Rusk, P.E.
Ms. Jennifer Pierce, UDRI
Mr. Wally Hoppe, UDRI
Mr. Brent Lancaster, ESRD, Inc.
Dr. Ricardo Actis, ESRD, Inc.
Dr. Barna Szabo, ESRD, Inc.

5d. PROJECT NUMBER

5e. TASK NUMBER

5f. WORK UNIT NUMBER

7. PERFORMING ORGANIZATION NAME(S) AND ADDRESS(ES)

Structures Division, Code 4.3.3
Bldg. 2187 Suite 2340A
Naval Air Systems Command
48110 Shaw Road, Unit #5
Patuxent River, MD 20670-1906

University of Dayton Research Institute
Structural Integrity Division
300 College Park
Dayton, OH 45469-0120

ESRD, Inc.
111 West Port Plaza, Suite 825
St. Louis, MO 63146-3109

8. PERFORMING ORGANIZATION REPORT NUMBER

NAWCADPAX/TR-2008/9

9. SPONSORING/MONITORING AGENCY NAME(S) AND ADDRESS(ES)

Office of Naval Research
One Liberty Center
875 North Randolph St., Suite 1425
Arlington, VA 22203-1995

10. SPONSOR/MONITOR'S ACRONYM(S)
ONR 3.5.1

11. SPONSOR/MONITOR'S REPORT NUMBER(S)

12. DISTRIBUTION/AVAILABILITY STATEMENT

Approved for public release; distribution is unlimited.

13. SUPPLEMENTARY NOTES

14. ABSTRACT

The global maritime operating environment of U.S. Naval Aviation assets necessitates their prolonged exposure to severe corrosive environments. The resulting corrosion damage on flight critical structural components has a significant adverse impact on fleet readiness and total ownership costs. To address these issues, NAVAIR has initiated a multiyear research program to investigate and quantify the fatigue life reduction due to corrosion on high-strength steels, and to develop models and metrics to implement actionable maintenance criteria for corrosion damage. The service component selected for analysis and testing was the F/A-18C/D arresting shank (P/N 74A480617). Five arresting shanks that were rejected for depot-level rework due to excessive corrosion damage were shipped by the Boeing Co. in Mesa, Arizona, to NAVAIR for inspection. Of the five, three were selected for fatigue testing due to the severity of the corrosion present and their overall condition. The three arresting shanks that were tested all exhibited a significant degree of fatigue resistance to fleet induced corrosion damage. This would imply that improvements in service life intervals for arresting shanks may be possible if the corrosion-fatigue damage resistance can be adequately characterized. All three shanks that were tested exhibited critical fatigue failures due to fretting at the hook end. As a result, fretting fatigue should be considered the primary fatigue failure mode for service-damaged arresting shanks.

15. SUBJECT TERMS

F/A-18 Arresting Shank AF1410 High-Strength Steel Corrosion Fatigue Testing Fretting
University of Dayton Research Institute (UDRI) Engineering Software Research and Development (ESRD)

16. SECURITY CLASSIFICATION OF:			17. LIMITATION OF ABSTRACT	18. NUMBER OF PAGES	19a. NAME OF RESPONSIBLE PERSON
a. REPORT	b. ABSTRACT	c. THIS PAGE			David T. Rusk
Unclassified	Unclassified	Unclassified	SAR	70	19b. TELEPHONE NUMBER (include area code) (301) 342-9428

Standard Form 298 (Rev. 8-98)
Prescribed by ANSI Std. Z39-18

SUMMARY

The global maritime operating environment of U.S. Naval Aviation assets necessitates their prolonged exposure to severe corrosive environments. The resulting corrosion damage on flight critical structural components has a significant adverse impact on fleet readiness and total ownership costs. Much of the costs and inconvenience of corrosion damage repair can be traced to uncertainty over the severity of corrosion necessary to cause a significant reduction in the fatigue life of a damaged component. This uncertainty has resulted in qualitative maintenance criteria for corrosion damage repair that are difficult to implement in practice, and do not provide objective measures of the reliability and risk associated with continued flight operation.

To address these issues, NAVAIR has initiated a multiyear research program to investigate and quantify the fatigue life reduction due to corrosion on high-strength steels, and to develop models and metrics to implement actionable maintenance criteria for corrosion damage. In an effort to generate fleet-representative corrosion data, airframe components subject to operationally-induced corrosion damage were analyzed and fatigue tested to failure to assess the criticality of corrosion severity, and to provide data to substantiate the experimental and life prediction tools developed by the program. The component selected for analysis and testing was the F/A-18C/D arresting shank (P/N 74A480617). The shank is made of AF1410 steel, and has a history of incurring corrosion damage in the lateral damper sleeve region. The majority of arresting shanks in the fleet are removed from service due to corrosion damage in this and other locations.

Five arresting shanks that were rejected for depot-level rework due to excessive corrosion damage were shipped by the Boeing Co. in Mesa, Arizona, to NAVAIR for inspection. Of the five, three were selected for fatigue testing due to the severity of the corrosion present and their overall condition. The three arresting shanks that were tested all exhibited a significant degree of fatigue resistance to fleet induced corrosion damage. This would imply that improvements in service life intervals for arresting shanks may be possible if the corrosion-fatigue damage resistance can be adequately characterized. All three shanks that were tested exhibited critical fatigue failures due to fretting at the hook end. As a result, fretting fatigue should be considered the primary fatigue failure mode for service damaged shanks.

Contents

ACKNOWLEDGEMENTS

The authors wish to thank Mr. Glenn Werczynski and Mr. David Willey of the NAVAIR Structural Test Facility (AIR-5.2.9.4.1) at NAS Patuxent River for performing the arresting shank testing described in this report. The authors also wish to thank Mr. Eric Burke, formerly of the University of Dayton Research Institute, for his efforts in developing the replication and corrosion surface imaging procedures described in this report.

INTRODUCTION

The global maritime operating environment of U.S. Naval Aviation assets necessitates their prolonged exposure to severe corrosive environments. The resulting corrosion damage on flight critical structural components has a significant adverse impact on fleet readiness and total ownership costs. Much of the costs and inconvenience of corrosion damage repair can be traced to uncertainty over the severity of corrosion necessary to cause a significant reduction in the fatigue life of a damaged component. This uncertainty has resulted in qualitative maintenance criteria for corrosion damage repair that are difficult to implement in practice, and do not provide objective measures of the reliability and risk associated with continued flight operation.

To address these issues, NAVAIR has initiated a multiyear research program to investigate and quantify the fatigue life reduction due to corrosion on high-strength steels, and to develop models and metrics to implement actionable maintenance criteria for corrosion damage. In an effort to generate fleet-representative corrosion data, airframe components subject to operationally-induced corrosion damage were analyzed and fatigue tested to failure to assess the criticality of corrosion severity, and to provide data to substantiate the experimental and life prediction tools developed by the program. The component selected for analysis and testing was the F/A-18C/D arresting shank (P/N 74A480617). The shank is made of AF1410 steel, and has a history of incurring corrosion damage in the lateral damper sleeve region. The majority of arresting shanks in the fleet are removed from service due to corrosion damage in this and other locations.

METHODS

TEST SPECIMENS

Five arresting shanks that were rejected for depot-level rework due to excessive corrosion damage were shipped by the Boeing Co. in Mesa, Arizona, to NAVAIR for inspection. Of the five, three were selected for fatigue testing due to the severity of the corrosion present and their overall condition. Shank number PT0735 was rejected for excessive corrosion in the lateral damper sleeve region. No scheduled removal data were available for this part, so the number of fleet arrestments since the last overhaul is unknown. Shank number 0491 was rejected for excessive corrosion on the inboard forward lug faces, but also had significant corrosion in the damper sleeve region. This shank had 91 total arrestments, with no record of any overhauls being performed. Shank number PT0099 was rejected for excessive corrosion in the lateral damper sleeve region, and had 198 fleet arrestments since the last overhaul.

CORROSION PREPARATION AND CHARACTERIZATION

Surface preparation and characterization of the lateral damper sleeve region of the three shank test specimens was performed by the University of Dayton Research Institute. The area of interest within each shank was cleaned, photographed, and replicated using a dental impression-

making material. The corrosion found within shank PT0735 was characterized from the replicas using a white light interferometer (WLI).

Prior to cleaning the shanks, acetate replicas were made in small spots within corroded regions of the interior lateral damper sleeve regions to extract corrosion by-products from the surfaces. The corroded regions looked discolored with small amounts of thin red rust. Examples of what the regions of interest looked like upon receipt are shown in figure 1. Miniscule samples of oxide solids were removed on several acetate replicas. The solids were examined using x-ray spectroscopy techniques and found to contain oxides of several of the base metal constituents. Details of the oxide analysis can be found in appendix A.

Figure 1: Examples of Corrosion Found in the Damper Sleeve Region

The areas of interest inside the shanks were cleaned to remove corrosion by-product solids from the surfaces using Turco Rust Remover 4181L. The preferred technique used for cleaning AF1410 high strength steel follows Boeing Process Specification 12030 – Type III for alkaline cleaning of ferrous, nickel, cobalt, titanium, molybdenum alloys, and stainless steels (reference 1). This process calls for submerging samples in a 25%-70% concentrated solution of the Turco 4181L at approximately 190°F for 5 to 30 min. In this application, the Turco solution was delivered to the areas of interest at room temperature using soaked cloths packed tightly inside the damper sleeve region of the shanks. Without the heat catalyst, the solution was left for approximately 24 hr to be effective. The progress was monitored frequently and the solution reapplied as necessary until the surfaces visually looked cleaner. The surfaces exposed to the alkaline cleaner were flushed with tap water until the pH of the residuals was neutral. The clean surfaces were dried with a heat gun, wiped with ethyl alcohol, and redried.

A coordinate system was established for the interior lateral damper sleeve surfaces of the shank for reference when taking photographs and replicas. The coordinate system chosen is shown in figure 2. Photographs were taken inside the damper sleeve region using a transparency film with a printed scale, a mirror, a fiber optic light source, and digital camera. The transparency film, with cylindrical coordinates printed on it, was taped tightly against the inner diameter surfaces of the damper sleeve region for reference. A round mirror and a high intensity light was oriented to

reveal small sections of the damper sleeve surface at a time. Digital photographs were recorded from the image in the mirror. The mirror was incremented forward and around to provide overlap between images. This process was performed until the entire circumference and length of the inner diameter surface was imaged. The images were then stitched together to create a 2-D montage of the damper sleeve region for each shank. An example montage of images taken down the length of the damper sleeve region of PT0735 is shown in figure 3. This image shows some of the operationally-induced corrosion damage found in PT0735 after it was cleaned with Turco Rust Remover 4181L. Full images of all three shanks can be found in appendix B.

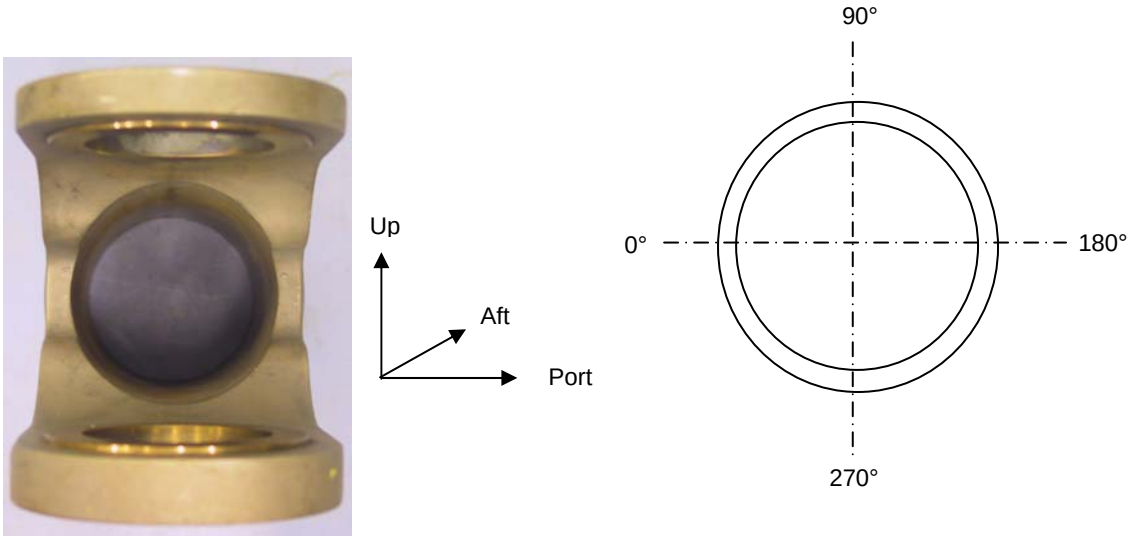

Figure 2: Coordinate System Established for Photographs and Replicas

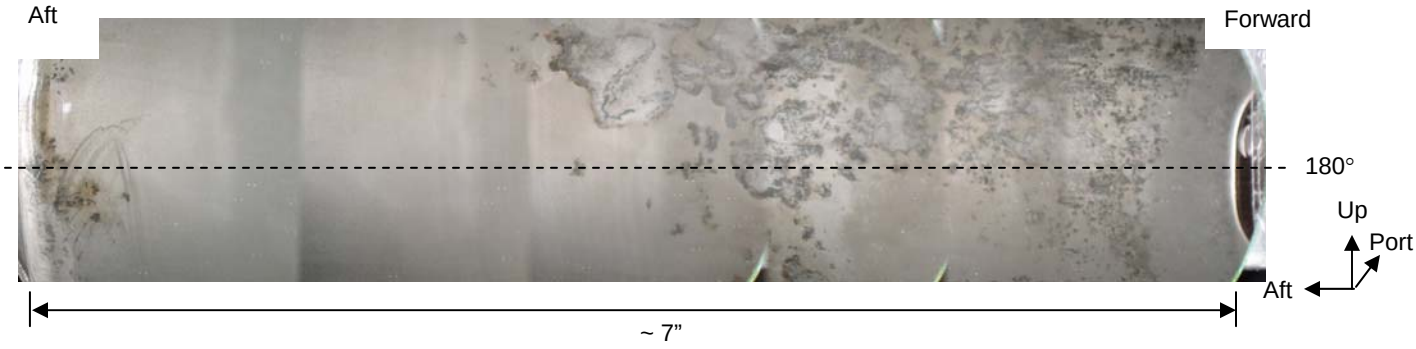

Figure 3: Montage of Images Taken the Length of the Damper Sleeve Region

Replicas of the surfaces in the damper sleeve region were obtained for all three shanks and were used for characterizing the corrosion within. Different replica making materials and techniques were researched for this application. A dental impression material (vinyl polysiloxane) was determined the best solution for obtaining the resolution required for corrosion characterization while being durable and easy to apply inside the damper sleeve of the shank. A description of the

materials selection process and testing of replication materials for use in this program can be found in the report "Navy High Strength Steel Corrosion-Fatigue Modeling Program" (reference 2). Instructions on how the replicas were created from the arresting shanks are included in appendix C.

Three separate replicas were used to replicate the damper sleeve region of a single shank. Each replica covered roughly 6 in. of length and 145 deg of circumference, allowing for 25 deg of overlap. PVC pipe with the appropriate outer diameter was cut into sections and used to back the replica and to create the impressions within the inner diameter of the damper sleeve region. A photograph illustrating how a replica impression was made in the shank is shown in figure 4. The dental impression material is orange in color and is between the shank surface and the PVC pipe section in the photograph.

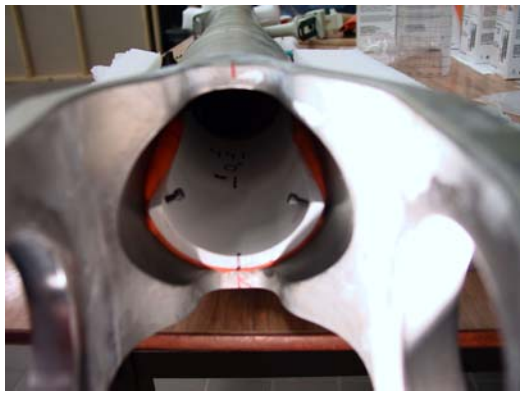

Figure 4: View of a Replica Being Made Inside the Damper Sleeve Region of the Shank

Measurements of the corrosion topography on the replica impressions from shank PT0735 were made at the University of Dayton Center for Materials Diagnostics using a WYKO NT-8000 WLI. When the instrument is setup for scanning the large shank replicas, the lateral resolution is approximately 3.8 microns and the vertical resolution is approximately 0.1 micron. The data were collected in 5mm x 5mm areas along the length of each replica. A highly accurate motorized stage incremented the replica under the objective lens by 4mm in order to allow lateral overlap between each 5mm x 5mm scan. Due to its curvature, once the small scanned areas covered the length of the replica, it had to be rotated under the objective lens of the interferometer using a rotating micrometer to focus on the next area. A photograph of a replica being measured using the WYKO NT-8000 in shown in figure 5. The replica is mounted on a specially designed fixture that holds the replica in place and rotates it about its center of rotation under the objective lens of the microscope.

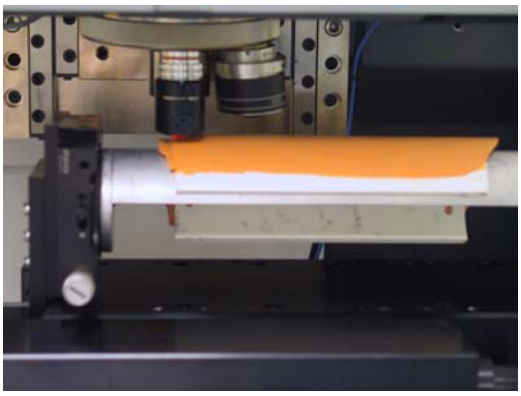

Figure 5: View of a Replica Mounted on a Rotating Fixture Being Inspected Using a White-Light Microscope

Postprocessing routines were utilized on the data to remove the cylindrical shape of the replica from the background, to stitch the data into a 2-D image, and to invert the depth information. The depth information from the replica was inverted since it is the impression of the surface. Deep, notch-like, features on the shank surface appear as high spots on the replica. When inverted, the depth information appears as it would if it were the actual corroded surface. An example of an area scan from a shank replica after it has been processed is shown in figure 6. The dark spots represent corrosion features.

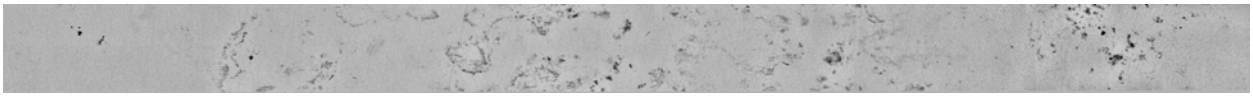

Figure 6: WLI Image of a Longitudinal Strip of Corrosion Damage on the Inner Damper Sleeve Region of an Arresting Shank

FINITE ELEMENT MODELING

Extensive finite element modeling (FEM) of the arresting shank was conducted by Engineering Software Research and Development, Inc. (ESRD), using their StressCheck® finite element software tool. Several different models were created, including a 2-D geometric nonlinear model, a full 3-D geometric nonlinear model, and a local 3-D model of the clevis assembly incorporating contact stresses. The full modeling effort is documented in the ESRD report "StressCheck Arrestment Hook Model Summary of Development and Validation Efforts," in appendix D.

LOAD SPECTRUM AND TEST SETUP

In an effort to determine the useful service life of F/A-18C/D arrestment shanks under load spectra that are representative of current fleet usage, a program to fatigue test uncorroded shanks to failure was conducted by Dayton T. Brown for NAVICP (reference 3). These tests involved

the cycling of the partial arresting hook assembly (P/N 74A480001), to include the arresting shank (P/N 74A480617), pivot assembly (P/N 74A480618) and arm assembly (P/N 74A480621). The lateral damper cylinder assembly (P/N 1B48040), bearing sleeve (P/N 74A480612) and hook point (P/N 74A480700) were not part of the tested assembly. A fatigue load spectrum, based on statistical analysis of available fleet survey data, was compiled by Ronkonkoma Aerospace Technologies, Inc. for the Dayton T. Brown test program (reference 4). The analysis divides the load spectrum into axial, side load, and vertical damper inputs for the three load cases of hook bounce, cable pickup, and drag load in a single aircraft arrestment event. Vertical damper loading has a varying resultant load angle because of differing shank angles with respect to the aircraft fuselage for the hook bounce and cable pickup load cases. These angles and the resulting load vectors were analyzed in reference 5. The final Dayton T. Brown fatigue test load spectrum assumes the carrier demonstration damper angles of 26.9 deg for hook bounce, and 48.4 deg for cable pickup.

For NAVICP testing, a 4-axis test frame using six hydraulic actuators was constructed to allow continuous combined application of loading inputs, to include axial loads, vertical damper loads, and side loads. Reproduction of this test frame for NAVAIR corrosion-fatigue testing was prohibitive from a cost and schedule perspective, so efforts were made to reduce the complexity of the load cases to simplify test frame geometry. The removal of side loading from the spectrum greatly simplified test fixturing, and a further simplification was to use a single damper angle for both hook bounce and cable pickup load cases, resulting in a 2-axis test frame with two hydraulic actuators. The critical load case for the damper region of the shank is cable pickup, so the cable pickup damper angle was also used for the hook bounce case in the NAVAIR testing. The hook bounce load magnitudes in the original spectrum were modified to apply a shank bending moment that would yield the same axial stress magnitude in the damper region as would be applied by the spectrum loads at the original damper angle. A stress reference point was chosen for this conversion to be 8.0 in. forward of the shank lateral pivot point, at the bottom of the inside diameter of the damper surface. Stresses for each load case were extracted from FEMs of the shank assembly. Axial stress at the reference point was estimated to be 74.6 ksi for the max hook bounce load of 18,500 lb at 26.9 deg. A schematic of the load application points on the test shank is shown in figure 7. A 3-D schematic and photos of the test fixture are included in appendix E. Peak load magnitudes and angles for the original NAVICP spectrum and the revised NAVAIR spectrum are listed in table 1. All testing was performed in the NAVAIR Structural Test Facility (AIR-5.2.9.4.1) at NAS Patuxent River, Maryland.

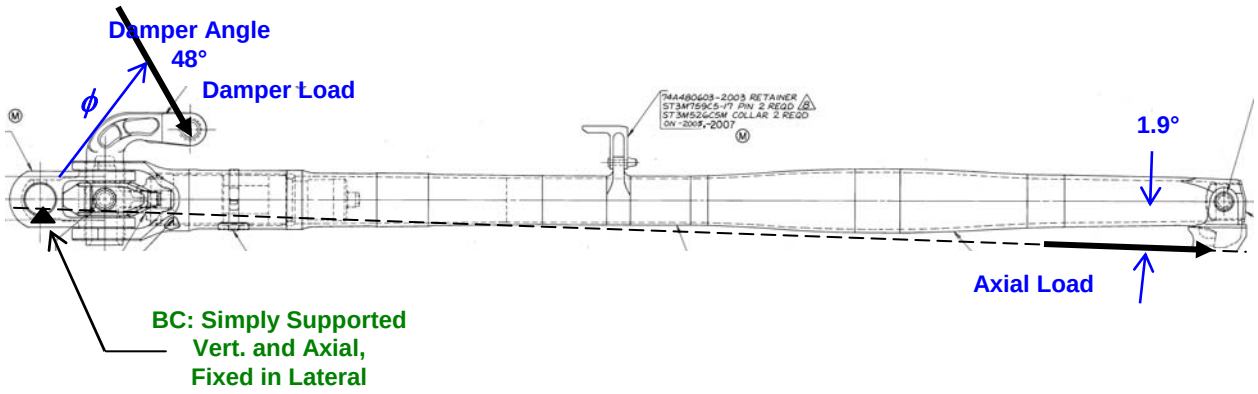

Figure 7: Applied Loads for NAVAIR Arresting Shank Fatigue Tests

Table 1: Peak Load Magnitude and Angle for Original and Revised Shank Spectrum

Spectrum	Load Case	Max. Load (lb)	Load Angle (deg)
Original (NAVICP)	Hook Bounce	18,500	26.9
	Cable Pickup	27,000	48.4
	Drag Load	133,000	-
Revised (NAVAIR)	Hook Bounce	15,750	48.4
	Cable Pickup	27,000	48.4
	Drag Load	133,000	1.9

Axial strain gages were applied to two shanks to perform strain surveys to validate FEM predictions in the damper region (figures 8 and 9). Shank number PT0099 had four gages installed 8.0 in. forward of the lateral pivot centerline at the top, bottom, and sides of the outer diameter. Uncorroded shank number 1277 was used for test fixture setup purposes, and had eight gages installed 8.0 in. forward of the lateral pivot centerline, with four gages placed identical to PT0099, and four spaced 30 deg apart from the others on the port side of the shank. All gages were oriented in the shank axial direction.

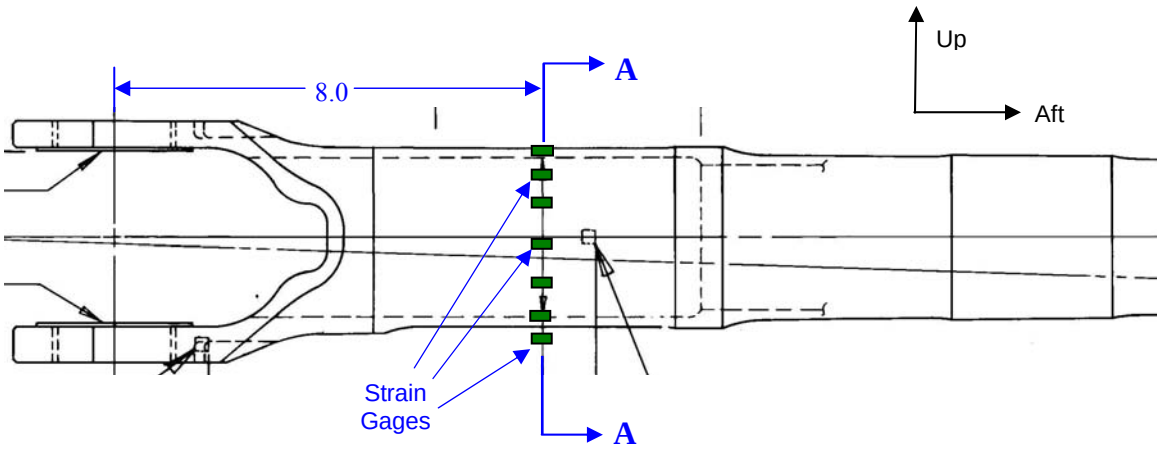

Figure 8: Axial Strain Gage Placement on Shank No. 1277

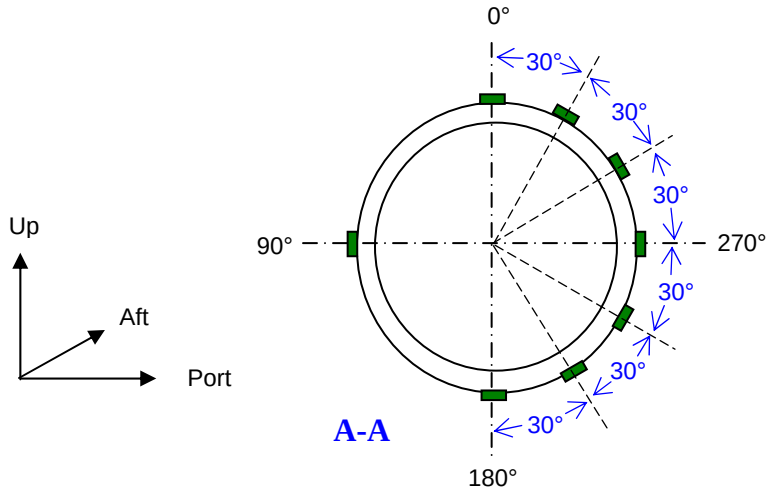

Figure 9: Axial Strain Gage Placement on Shank No. 1277 (Section A-A)

RESULTS

FINITE ELEMENT MODEL RESULTS

Results of the FEM predictions are listed in appendix D. Significant results extracted from the models were stresses and strains at the shank strain gage locations, and surface stress contour maps of the inside bore of the shank lateral damper region.

STRAIN SURVEY RESULTS

Several strain surveys were performed before fatigue testing of the corroded shanks to verify the stresses in the damper region, and to evaluate the fidelity of the FEMs. Damper load strain surveys were performed on shanks 1277 and PT0099, with the results for 1277 shown in figure 10.

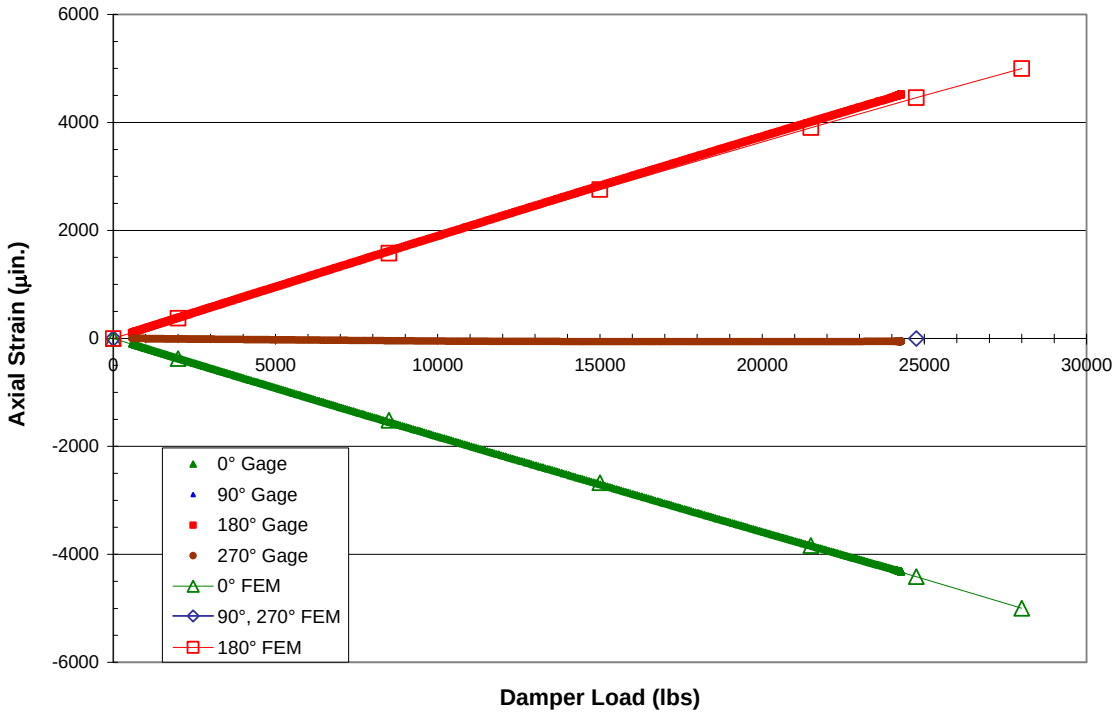

Figure 10: Damper Load Strain Survey Results (Shank No. 1277)

Numerical comparison of the measured strains versus the FEM predicted strains for damper loading are listed in table 2, for the maximum strain survey damper loading of 24,293 lb. Finite element values are linearly interpolated from the solution points shown in figure 10. Measured strain values are an average of three separate load applications.

Table 2: Strain Survey versus FEM results for Shank Damper Loading

Strain Gage Location (deg)	Average Measured Strain ($\mu in./in.$)	FEM Strain ($\mu in./in.$)	Error (%)
0	-4,312	-4,331	0.454
90, 270	-53	-0.21	-
180	4,514	4,381	-2.95

Axial load strain surveys were performed on shanks 1277 and PT0099, with the results for 1277 shown in figure 11 for a peak axial load value of 136,900 lb.

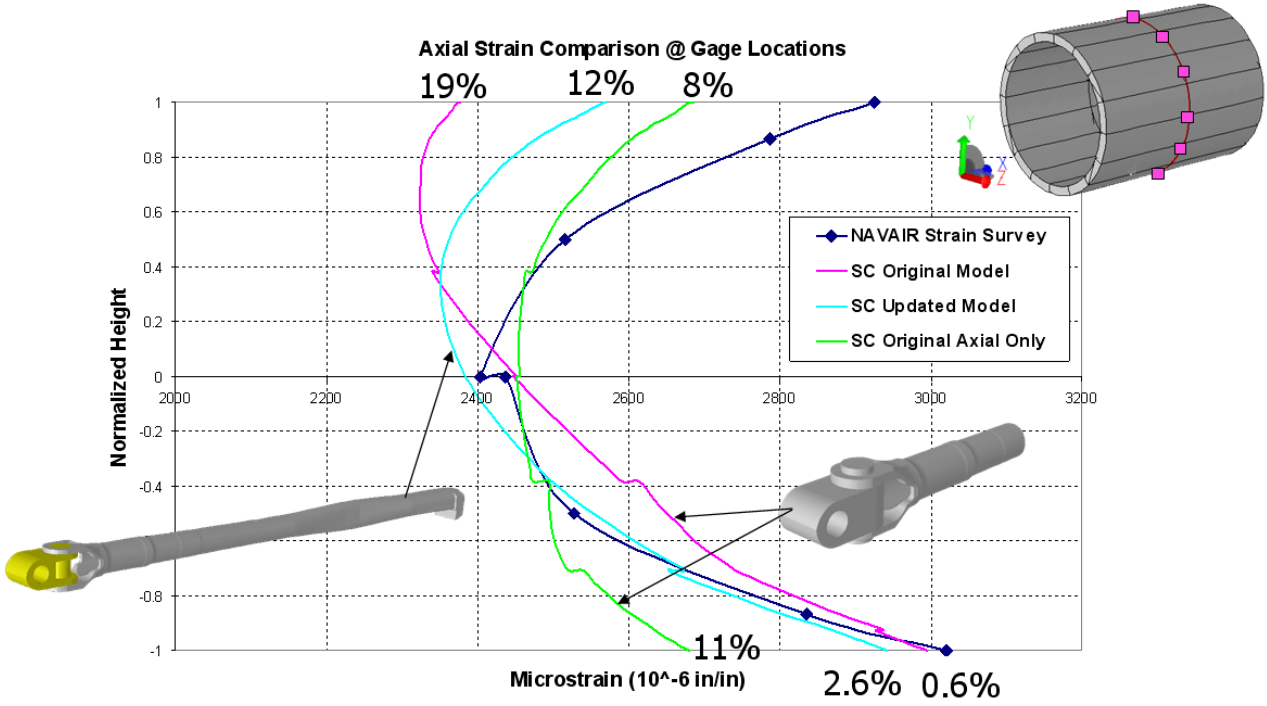

Figure 11: Axial Load Strain Survey Results (Shank No. 1277)

Axial survey results show a nonlinear strain distribution through the damper region cross-section which was not predicted by the initial 2-D nonlinear FEM. A similar strain response was also found in the surveys on shank PT0099, indicating that the measurements were not the result of individual gage anomalies or placement variation. Further analysis by ESRD concluded that the 2-D geometric nonlinear model gave inaccurate bending moment values in the damper region under axial load. The limiting case of zero bending moment under axial load was run using the local 3-D model incorporating contact stresses, with the results plotted in figure 11. The updated full 3-D geometric nonlinear model results are also plotted in figure 11 for comparison, and show that the stress distribution in the lower half of the shank is modeled quite accurately, but still contains about 12% relative error in the upper half of the shank. The source of the error is

the current inability of StressCheck® to model contact stresses in a 3-D geometric nonlinear analysis. The cross-sectional stress distribution at the strain gage locations shows a significant through-thickness stress gradient at the top and bottom of the shank, due to the load transferring through the clevis (figure 12).

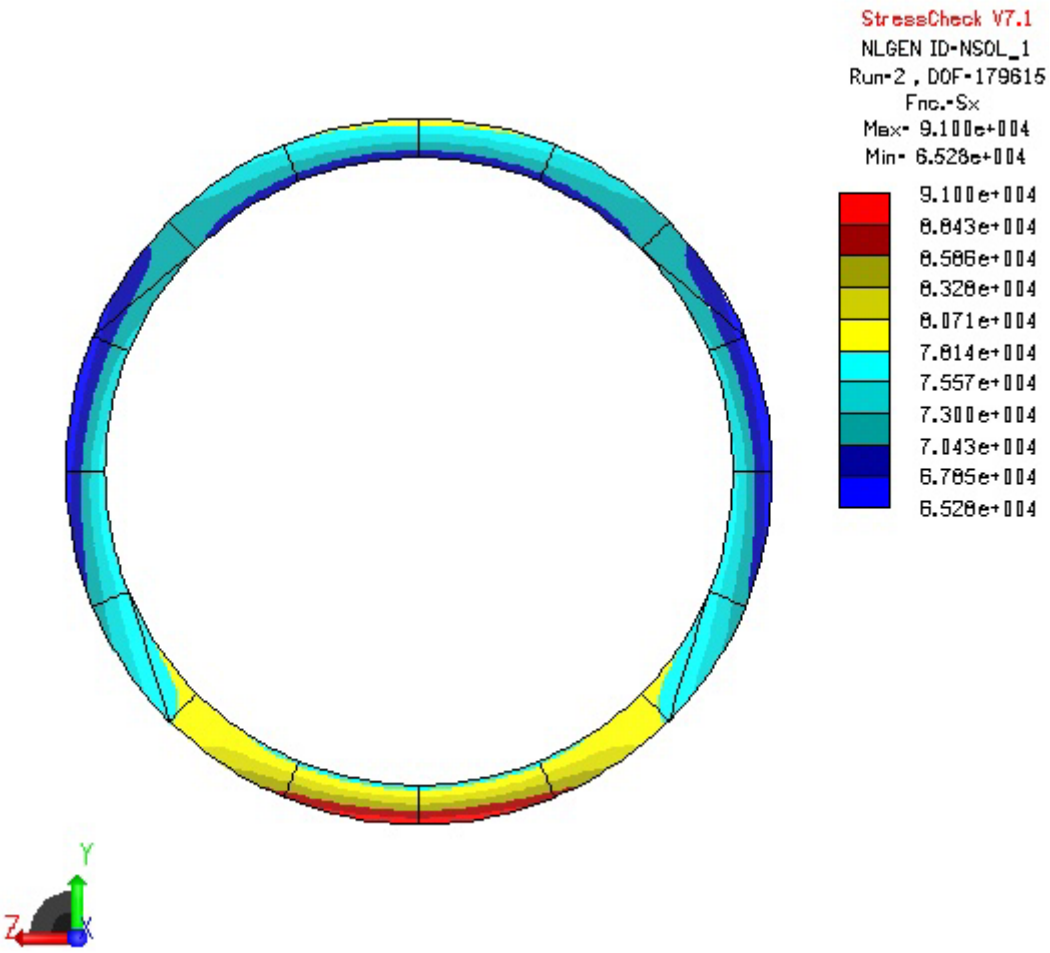

Figure 12: Stress Contours of Shank Cross-Section at Strain Gage Locations, Under Axial Loading

For the corrosion investigation of AF1410, the primary region of interest on the arresting shank is the inside diameter of the damper region. Here, the peak stresses were relatively insensitive to changes in bending moment and clevis constraints of the various models (less than 1% error). Therefore, the revised model was considered sufficient for the purposes of this research program. Further details of the strain survey analysis are listed in appendix D.

Numerical comparison of the measured strains versus the FEM predicted strains for axial arrestment loading are listed in table 3, for the maximum strain survey axial load of 136,745 lb. Measured strain values are an average of three separate load applications.

Table 3: Strain Survey versus Updated FEM Results for Axial Arrestment Loading

Strain Gage Location (deg)	Average Measured Strain ($\mu in./in.$)	FEM Strain ($\mu in./in.$)	Error (%)
0	2,922	2,570	12.0
90, 270	2,415	2,380	1.4
180	3,017	2,940	2.6

FATIGUE TEST RESULTS

Shank PT0099 failed at 11,089 test spectrum arrestments. The failure location was 1.3 to 1.8 in. forward from the load bearing face of the hook point, at the bottom of the shank tube (figures F-1 and F-2). Two primary crack origins are present on the fracture surface. Crack 1 is 1.3 in. forward from the hook point, and originates from localized surface roughness, as shown in figure F-3. The final crack depth is 0.81 in. Crack 2 is 1.8 in. forward from the hook point, and originates from a scratch that is nearly perpendicular to the loading direction (figure F-5). The final crack depth is 1.27 in. Significant fretting damage is evident on the shank surface in the region of cracks 1 and 2. Multiple secondary crack initiation locations are also visible on the fracture surfaces of cracks 1 and 2 (figures F-4 and F-6).

Shank 0491 failed at 9,811 test spectrum arrestments. The failure location was 12.68 in. forward from the load bearing face of the hook point, at the bottom of the shank tube (figures F-7 and F-8). The primary crack origin is a surface scratch approximately 30 deg off of an axis normal to the loading direction, as shown in figure F-9. The final crack depth is 0.92 in. Indications of mild fretting damage are visible on the shank surface in the region of the fatigue crack (figure F-10).

Shank PT0735 failed at 7,413 test spectrum arrestments. The failure location was 1.35 in. forward from the load bearing face of the hook point, at the bottom of the shank tube (figures F-11 and F-12). The primary crack originates from an area of localized surface roughness, as shown in figure F-13. The final crack depth is 0.84 in. Examination of the fracture surfaces shows that the crack initiated at multiple sites along the bottom surface of the shank in locations where there is a significant amount of fretting damage (figure F-14).

At the completion of fatigue testing, the shanks were destructively sectioned in the lateral damper region to expose the corrosion damage on the inside diameter. Each shank section was then subjected to a magnetic particle inspection in the damper region to look for cracks that may have initiated during testing, but did not grow to critical size. No evidence of cracking was found in any of the shank sections that were examined. However, two fatigue cracks were found on shank PT0099 at 1.55 in. and 1.65 in. forward of the lateral damper sleeve inside diameter fillet (figures F-15 and F-16). The cracks are at the bottom of the shank, and initiated from an area of significant corrosion damage on the inside bore (figures F-17 and F-18). The light colored material wedged in the open crack is replicating material left over from the replicating process.

Both cracks broke through to the outer surface of the shank, but did not grow to critical size before the shank failed at the hook end (figures F-19 and F-20). The crack origins are from large, shallow pit-like features where significant amounts of surface material have been corroded away, leaving a roughened surface behind. The depths of the corrosion features that caused the cracks are 0.0138 in. (0.351 mm) for crack 1 (figure F-21) and 0.0223 in. (0.566 mm) for crack 2 (figure F-22). No discernable marker features were found on the fracture surfaces of either crack.

DISCUSSION

The F/A-18C/D arresting shanks that were rejected for depot-level rework and sent to NAVAIR are assumed to be a representative sample of the type and level of corrosion damage that is typically incurred by these components under operational conditions. As such, the detailed information of the corrosion topology derived from the WLI measurements should be adequate to develop models that assess the severity of corrosion damage with respect to fatigue life. The revised 3-D FEM of the shank is considered to be refined enough to accurately capture the stresses on the inside surface of the damper sleeve region. Use of these models for stress and strain analysis outside the damper sleeve region should be done cautiously, especially in the clevis region where known inaccuracies exist in the modeling of contact stresses.

Elimination of side loading on the arresting shank test fixture is not expected to have an effect on the fatigue behavior of the corroded lateral damper region, since the stresses in that region are dominated by the axial and vertical bending loads. Shank side loading primarily affects the stresses at the hook end, which is not the region of interest for this test program. Since all three shanks tested exhibited critical fatigue failures due to fretting at the hook end, fretting fatigue should be considered the primary fatigue failure mode for service damaged shanks. The lack of a critical fatigue failure due to corrosion indicates that there is a significant capacity for fatigue damage resistance in corrosion-damaged shanks. This would imply that improvements in service life intervals for arresting shanks may be possible if the corrosion-fatigue damage resistance can be adequately characterized. The corrosion damage on shank PT0099 that led to noncritical fatigue cracking was more severe than the damper sleeve corrosion on all three of the shanks that were tested. It is unclear if the corrosion damage on shank PT0099 represents an extreme case, or if it is more typical of the corrosion seen in depot-level inspections. Shank 0491 and PT0735 had only mild amounts of corrosion forward of the lateral damper sleeve inside diameter fillet.

THIS PAGE INTENTIONALLY LEFT BLANK

CONCLUSIONS

The AF1410 steel F/A-18C/D Arresting Shank has demonstrated, in laboratory testing, a significant degree of fatigue resistance to fleet induced corrosion damage. This would imply that improvements in service life intervals for arresting shanks may be possible if the corrosion-fatigue damage resistance can be adequately characterized. All three shanks that were tested exhibited critical fatigue failures due to fretting at the hook end. As a result, fretting fatigue should be considered the primary fatigue failure mode for service damaged shanks.

THIS PAGE INTENTIONALLY LEFT BLANK

REFERENCES

1. P.S. 12030, “Process Specification: Cleaning, Alkaline,” The Boeing Company, St. Louis, MO, of 23 Apr 1999.

2. UDR-TR-2007-00039, “Navy High-Strength Steel Corrosion-Fatigue Modeling Program,” University of Dayton Research Institute, Dayton, OH, of Oct 2006.

3. Kelley, S., “Test Report for F-18 Hook Shank Assembly, Part No. 74A480617, Full Scale Fatigue Test and Crack Growth Coupon Test Programs,” Report No. DTB02R03-0858, Dayton T. Brown, Inc., of 25 Nov 2003.

4. Memorandum from P. Bell, “F-18 Arresting Hook Shank Full-Scale Test Loads and Spectrum,” Ronkonkoma Aerospace Technologies, Inc., of 11 Oct 2000, Revised 5 Feb 2001.

5. Bell, P., “F-18 Hook Shank Full Scale Fatigue Test Damper Load Angle Review,” Report No. RAT01-020, Ronkonkoma Aerospace Technologies, Inc. of 15 Dec 2001.

THIS PAGE INTENTIONALLY LEFT BLANK

APPENDIX A
ANALYSIS OF F/A-18C/D ARRESTING SHANK CORROSION OXIDES

Prior to cleaning the F/A-18C/D arresting shanks, acetate replicas were made in small spots within corroded regions of the interior lateral damper sleeve regions to extract corrosion by-products from the surfaces. The corroded regions looked discolored with small amounts of thin red rust. Miniscule samples of oxide solids were removed on several acetate replicas. The solids were examined using x-ray spectroscopy techniques and found to contain oxides of several of the base metal constituents. See figure A-1 for an example of the results from the x-ray analyses performed on the solids removed from the corroded surface. The images in figure A-1(a) were obtained from a scanning electron microscope (SEM) with electron dispersive X-ray (EDX) analysis capability. The SEM image is on the left and the results from the EDX are show as an overlay on the image for each element identified. Light pixels represent the detection of the element of interest. The chart and plot in figure A-1(b) provide semi-quantitative results for the elements detected via X-ray fluorescence spectroscopy.

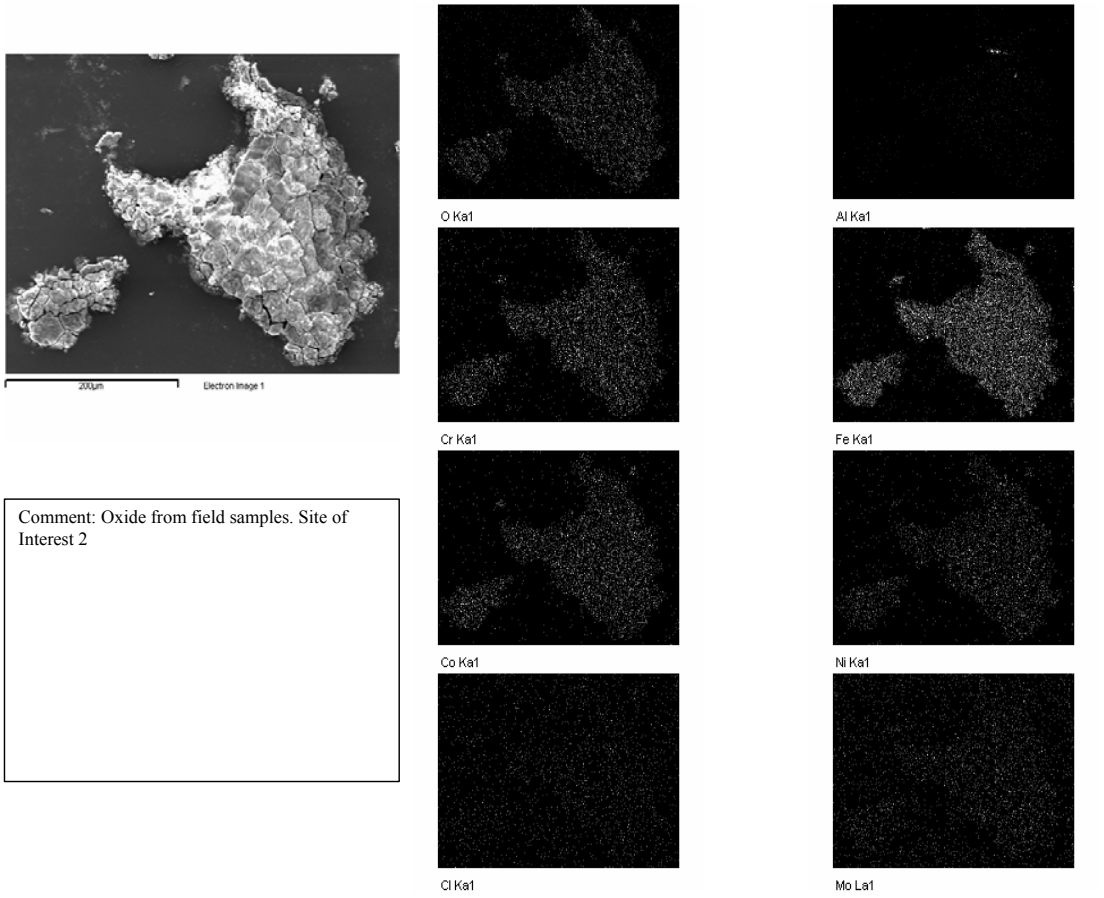

Comment: Oxide from field samples. Site of Interest 2

Spectrum processing :
No peaks omitted

Processing option : All elements analyzed (Normalised)
Number of iterations = 3

Standard :
O SiO2 1-Jun-1999 12:00 AM
Al Al2O3 1-Jun-1999 12:00 AM
Cr Cr 1-Jun-1999 12:00 AM
Fe Fe 1-Jun-1999 12:00 AM
Co Co 1-Jun-1999 12:00 AM
Ni Ni 1-Jun-1999 12:00 AM
Mo Mo 1-Jun-1999 12:00 AM

Element	Weight%	Atomic%
O K	40.76	69.19
Al K	4.43	4.46
Cr K	7.28	3.80
Fe K	30.54	14.85
Co K	8.66	3.99
Ni K	7.51	3.47
Mo L	0.83	0.23
Totals	100.00	

Comment: Oxide from field samples. Site of Interest 2

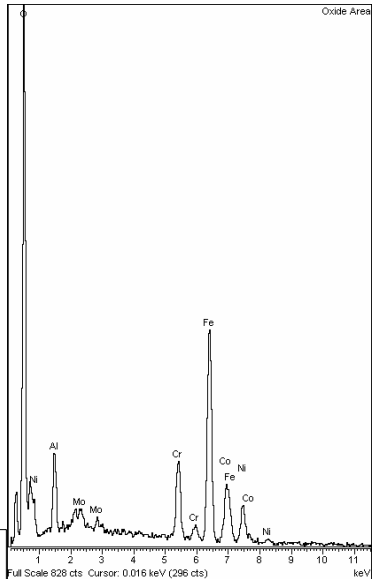

Figure A-1: X-ray Analysis of Oxides Removed from the Damper Sleeve Region (a) Images and Results from a SEM with EDX Capability (b) Results from an X-ray Flourescence Spectrometer

APPENDIX B
PHOTO MONTAGE OF CORROSION ON THE INSIDE LATERAL DAMPER REGION OF THREE F/A-18C/D ARRESTING SHANKS

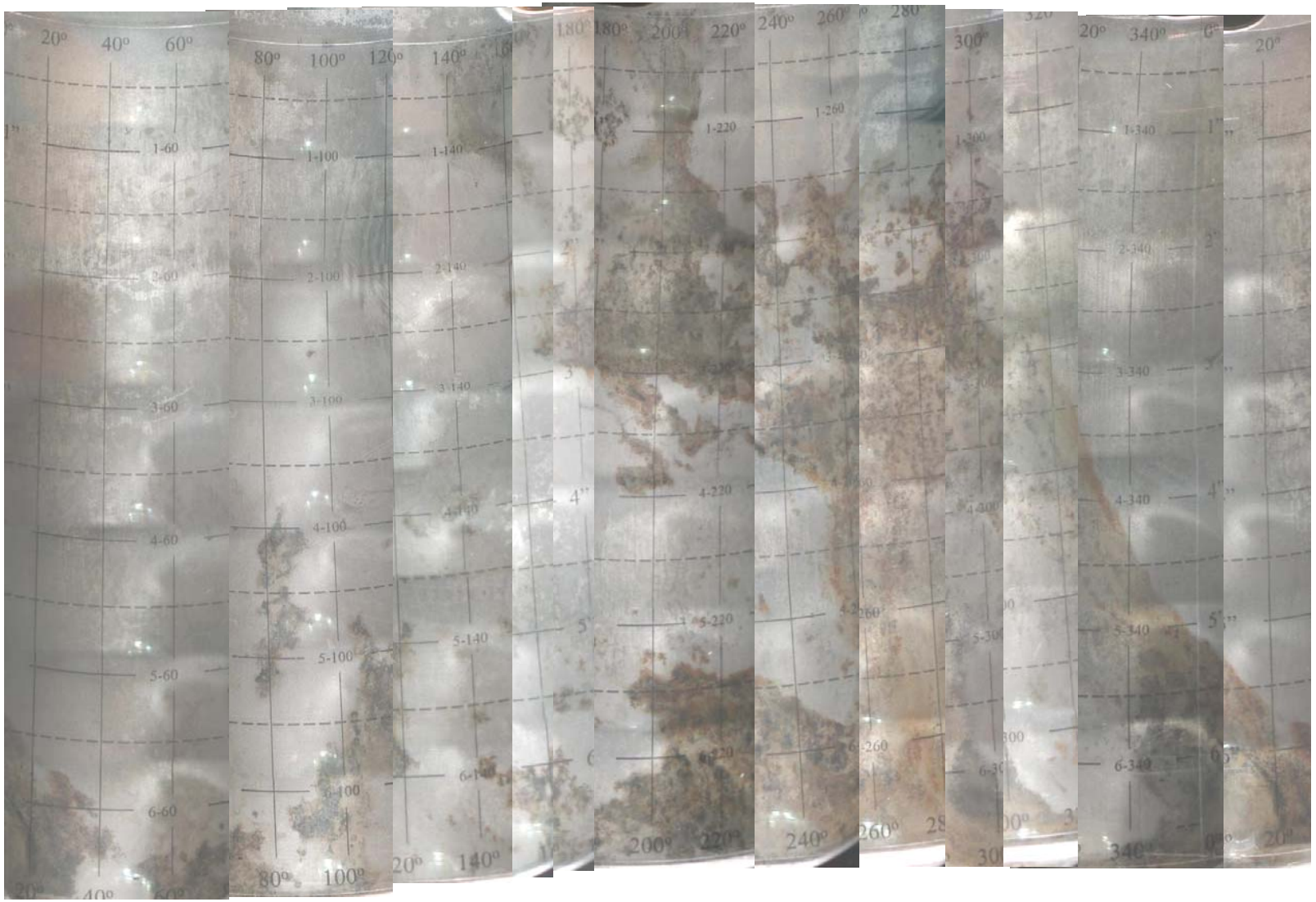

Figure B-1: Photo Montage of Corrosion on Inside Damper Region of Shank PT0099

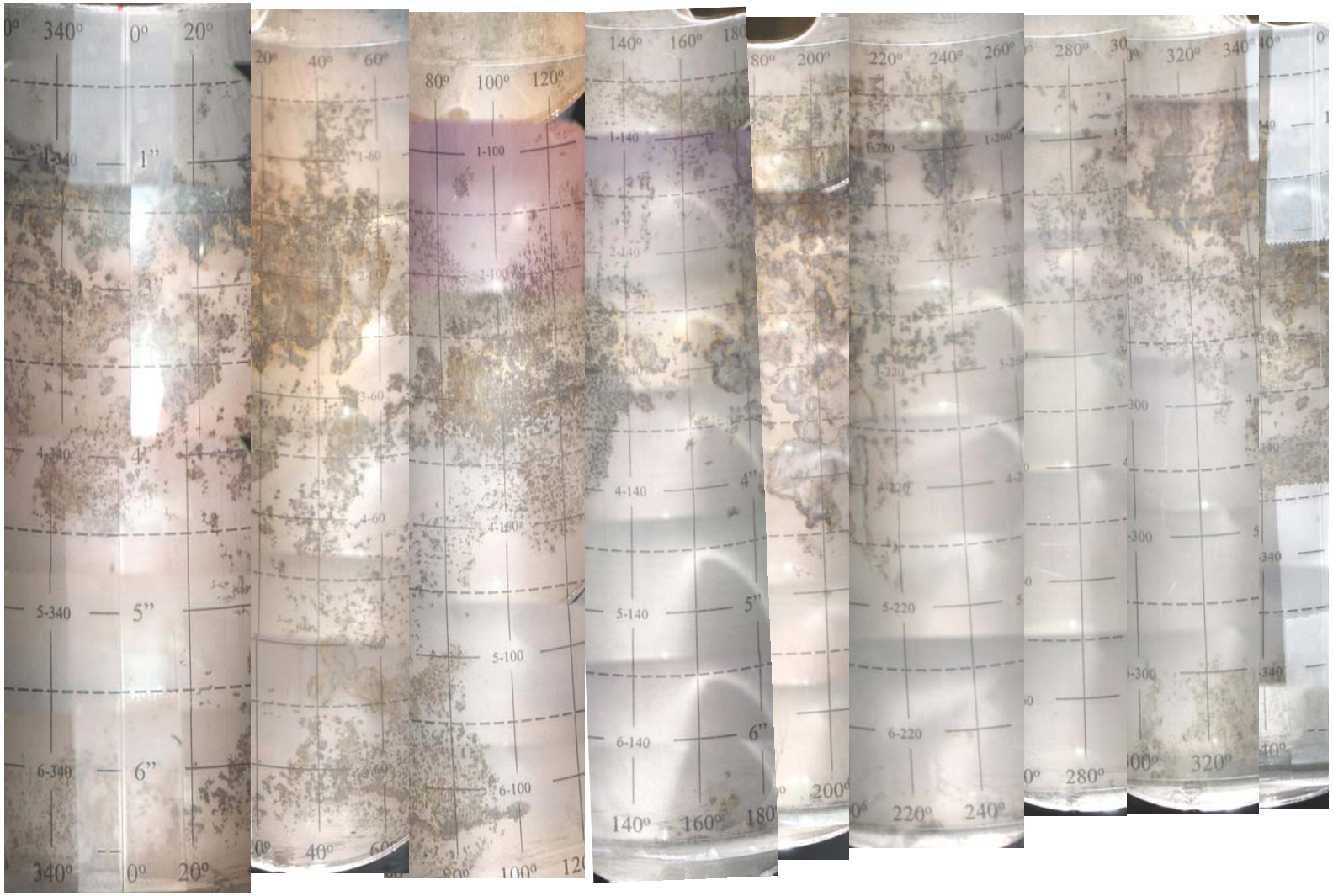

Figure B-2: Photo Montage of Corrosion on Inside Damper Region of Shank PT0739

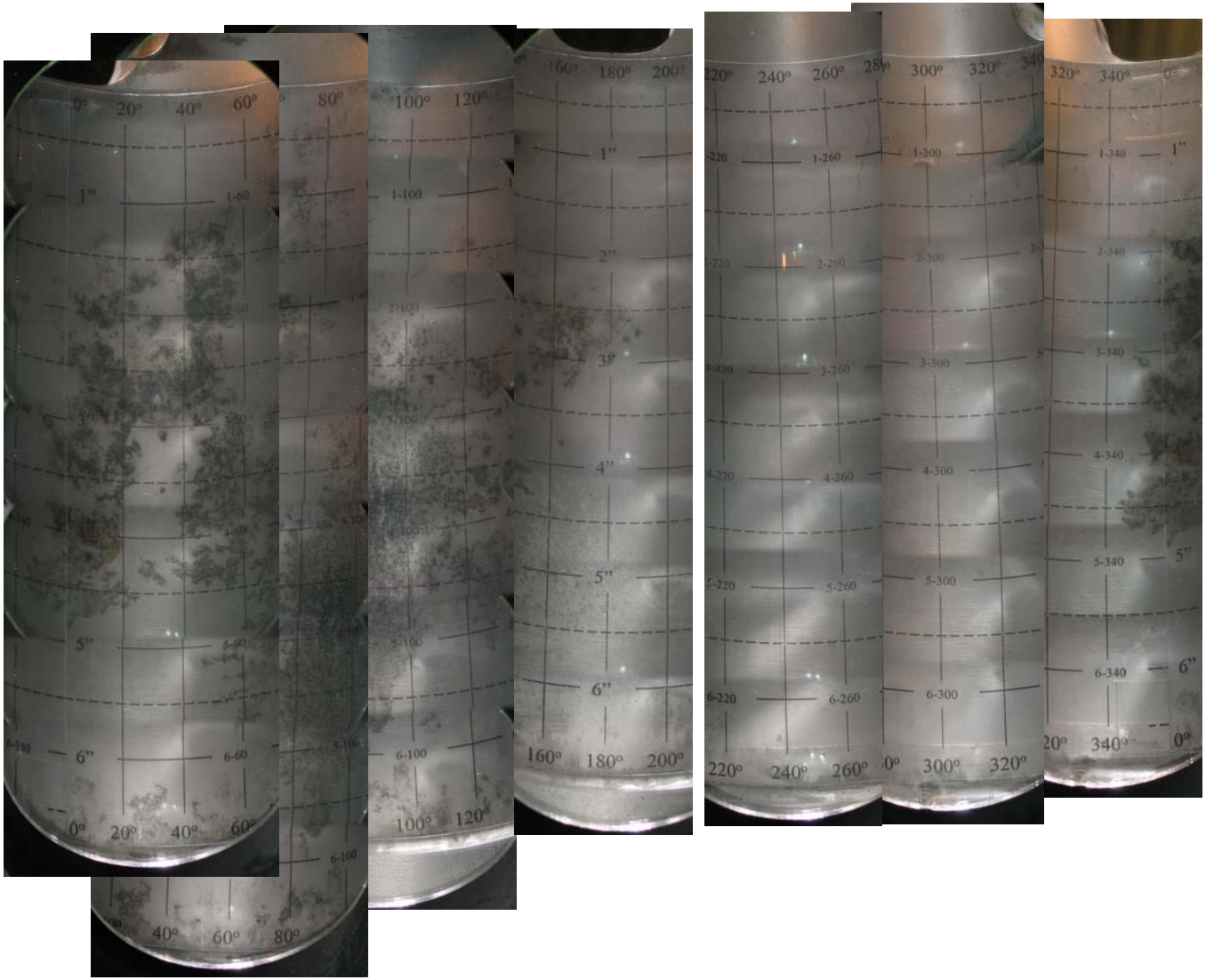

Figure B-3: Photo Montage of Corrosion on Inside Damper Region of Shank 0491

APPENDIX C
PROCEDURES USED FOR REPLICATING CORRODED SURFACES IN THE DAMPER SLEEVE REGION OF F/A-18C/D ARRESTING SHANKS

SUPPLIES NEEDED

Aquasil Ultra XLV
2½ in. Schedule 40 PVC Pipe
(4) #4-40 x ½ Socket Head Cap Screws
Large Pry Bar
120 Grit Sandpaper
Piece of PVC Pipe cut to approximately 95 deg Arc

PROCEDURE

Cut PVC pipe into 6 in. lengths, then cut lengthwise to produce pieces of about 145 deg arc. This will create enough overlap to allow the entire ID of the shank to be replicated with three molds. Near the ends of the PVC pieces, and as close to the edges as possible, drill and tap four holes for #4-40 screws. (Since these tapped holes will only get used once a larger drill bit than specified can be used. This makes it easier to thread the screws in by hand and to adjust their depth.) See figure C-1 for a photo of a PVC section ready to be used for replication of the shank. Roughen the outer surface of the PVC with sandpaper to help the replica material adhere to the PVC. File down sharp edges and wipe the pieces off thoroughly to prevent foreign material from getting onto the molded surface.

Figure C-1: Photo of a PVC section that has been prepared for replication of the shank

Check the surface to be replicated for any dirt or foreign material and clean as needed. Mark 0, 120, and 240 deg on the arrestment shank, working clockwise from 0 deg.

Insert screws into a piece of PVC pipe and adjust the depth of the screws to allow approximately 3/32 in. between the shank and the PVC when it is put in place. Be careful when inserting and removing the PVC from the shank not to scratch the surface of the shank. Figure C-2 illustrates how the PVC section should look when in place inside the shank.

Figure C-2: Photo of a PVC section inserted into place within the shank

Remove the PVC from the shank. Mark the inner surface of the PVC with the shank serial number, position of the mold, and the mold number (we make two molds of each area).

Install a cartridge of Aquasil Ultra XLV in the application gun, remove the cap, and install a mixing nozzle on the cartridge. A photograph of the loaded application gun is shown in figure C-3.

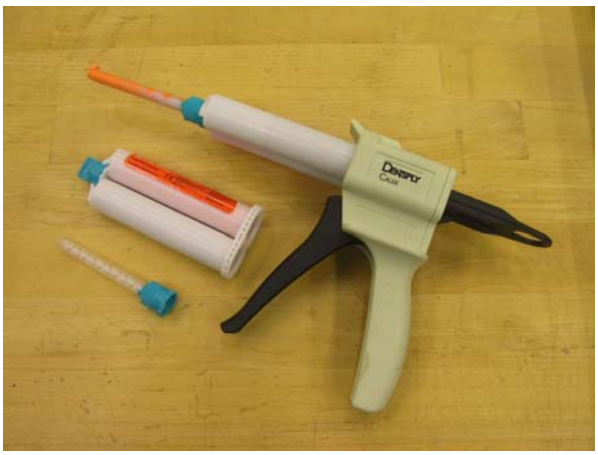

Figure C-3: Photo of an application gun with Aquasil Ultra cartridge and mixing tube

Once mixed, the working time of the Aquasil is only 2 min and 15 sec so the next steps must be performed as quickly as possible. Squeeze the Aquasil onto the surface to be replicated, trying to spread it fairly evenly. Use the entire cartridge to ensure adequate coverage. Place the PVC over the Aquasil with the PVC roughly centered on the alignment mark on the shank. Press the PVC into the Aquasil by hand. The PVC will tend to float on the Aquasil so care must be taken to prevent the PVC from sliding very far either front-to-back or side-to-side. Place the smaller piece of PVC so that it rests on the screw heads. (If the weight is placed directly on the PVC mold backing, it can flex enough to bottom out on the surface of the shank. The smaller piece of PVC transfers the weight directly through the screws.) Support the large end of the pry bar and insert the small end into the shank until the end is approximately halfway along the top piece of PVC. Rest the pry bar on the PVC and exert enough downward force to ensure that the screw tips are in contact with the shank. See figure C-4 for an illustration of the method used to apply pressure to the PVC backing using a large bar.

Figure C-4: Illustrates how pressure to the PVC backing is applied using a large bar

Allow the Aquasil to cure for 10 min. Remove the pry bar and the small piece of PVC. Carefully use a razor blade to remove excess replica material from the exposed end of the mold.

With an indelible pen, mark the end of the mold to correspond with the mark on the shank. Photograph the marks for future reference. See figure C-5 for an example of how the replica should be marked and photographed before removing it from the shank.

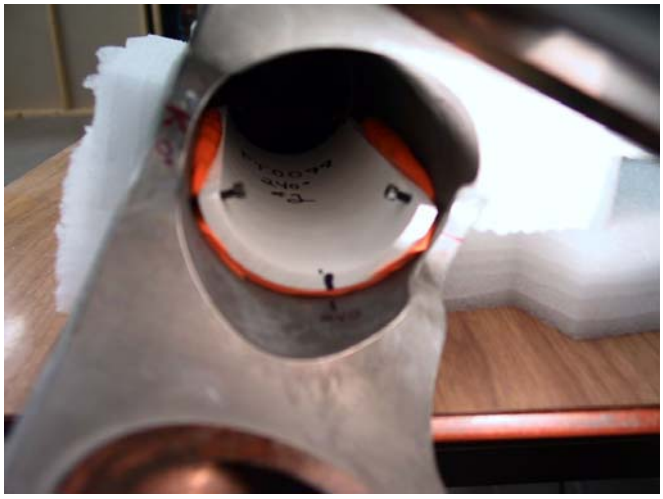

Figure C-5: Example of how the replica should be marked and photographed before removing.

Carefully pry the mold away from the shank. Make sure that the replica peels away from the shank and not from the PVC backing. Remove the cast from the shank – DO NOT REMOVE FROM PVC BACKING OR TOUCH THE SURFACE OF THE IMPRESSION AFTER THE CAST HAS BEEN MADE. With a razor blade, carefully trim excess replica from the sides of the cast.

Mark a plastic bag with the shank serial number, position of the replica, and the replica number. Place the PVC backed replica in the bag replica side up and seal.

APPENDIX D
ENGINEERING SOFTWARE RESEARCH AND DEVELOPMENT, INC. REPORT

COPY

StressCheck Arrestment Hook Model
Summary of Development and Validation Efforts
Validation Task #9
June 27, 2007
Report Prepared By: Brent Lancaster, Ricardo Actis and Barna Szabo

1) Introduction

ESRD performed finite element analyses of the AF1410 arrestment hook shank, for typical arrestment and hook bounce load cases, with the purpose of determining the stress distribution for a specific region inside the bore of the shank. For each load case, the prediction of the strains at gage locations was compared against experimental strain data provided by NAVAIR. For each load case, a working model was constructed to determine the strain and stress distributions in the region of interest. For the arrestment load case, the original model was not acceptable because it could not represent the strain-gage test data well (see Section 4). The model was revised and the results compared with the experimental data. The modeling approaches, assumptions and FEA results are described in the following. The p-version FEA code StressCheck was used for all of the calculations. The geometric description of the arrestment shank was obtained from drawings provided by NAVAIR (reference drawings 74A480001 and 74A480617), and the following material properties were used for the analyses: E=29.4e6 psi, □=0.31.

2) Modeling Case 1: Arrestment Load

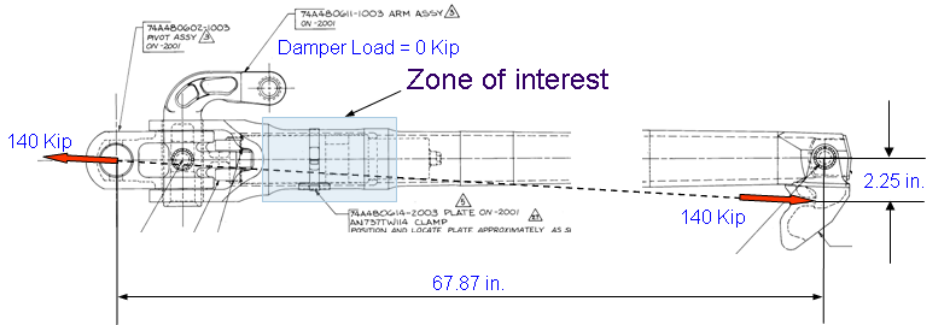

Figure 1: Arrestment load case configuration

2.1) Modeling Approach and Results

In the arrestment load case, a 140 kip axial load is applied to the hook end and reacted through the assembly connection. The working model consisted in a 2-D representation of the complete shank to determine the moment (M), shear (V) and normal (N) forces at a location close to the region of interest (Section B-B in Figure 2).

COPY

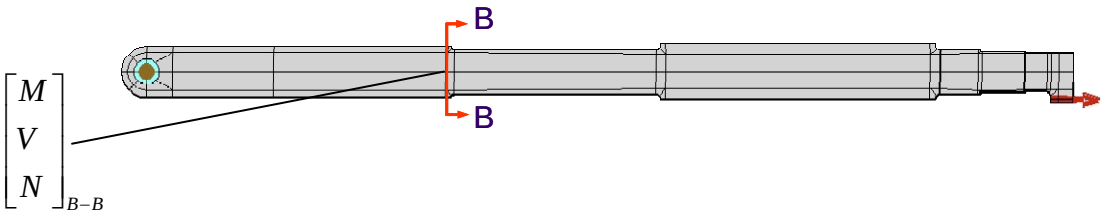

Figure 2: 2-D representation of the tail hook for the arrestment load case.

In this 2-D model (plane strain) the height and thickness of each section was determined so as to maintain the same cross-sectional area and moment of inertia of the different regions of shank. Figure 3 shows the thickness variation to accomplish this. This model is appropriate to obtain the deformed configuration, the moment, axial force and shear force at Section B-B.

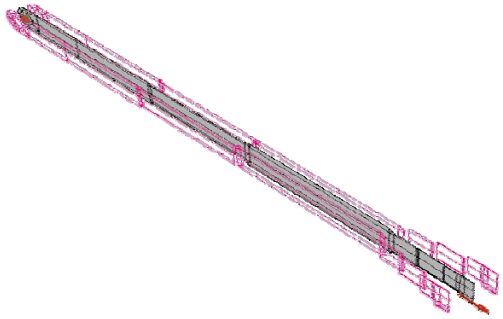

Figure 3: Thickness variation for the 2-D model of the tail hook.

The prescribed boundary conditions for the 2-D representation of the arrestment load case are given in Figure 4. A fastener element was used to simulate the pinned connection while a distributed traction was used to apply an axial load of 140100 lb to the hook end. A nodal constraint was used to prevent rigid body motion (RBM). The center of the fastener was constrained in two orthogonal directions.

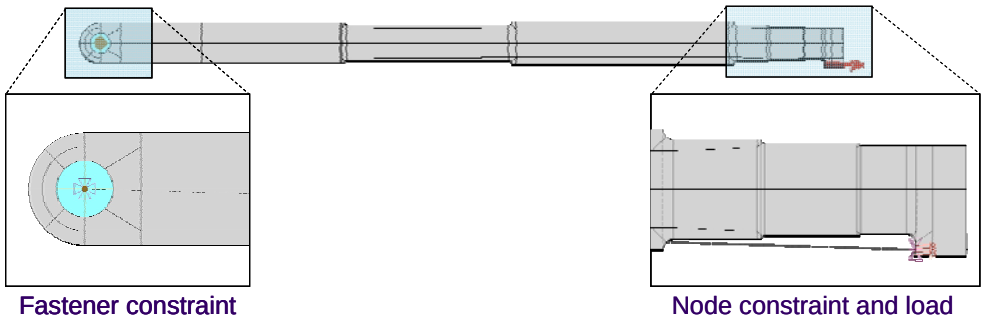

Figure 4: Boundary conditions for 2-D representation of the arrestment load case.

First, a linear analysis was performed by p-extension. After a linear analysis was performed, it was determined from the results that geometric nonlinear effects could not be ignored. Therefore, a geometric nonlinear analysis was performed in order to account for the redistribution of load due to the coupling between axial and bending. The moment diagram and vertical displacements for the linear and geometric nonlinear solutions are shown in Figure 5. Additionally, the moment, shear force and normal force at Section B-B located at 22.4-in from the center of the fastener are shown in the table of Figure 5.

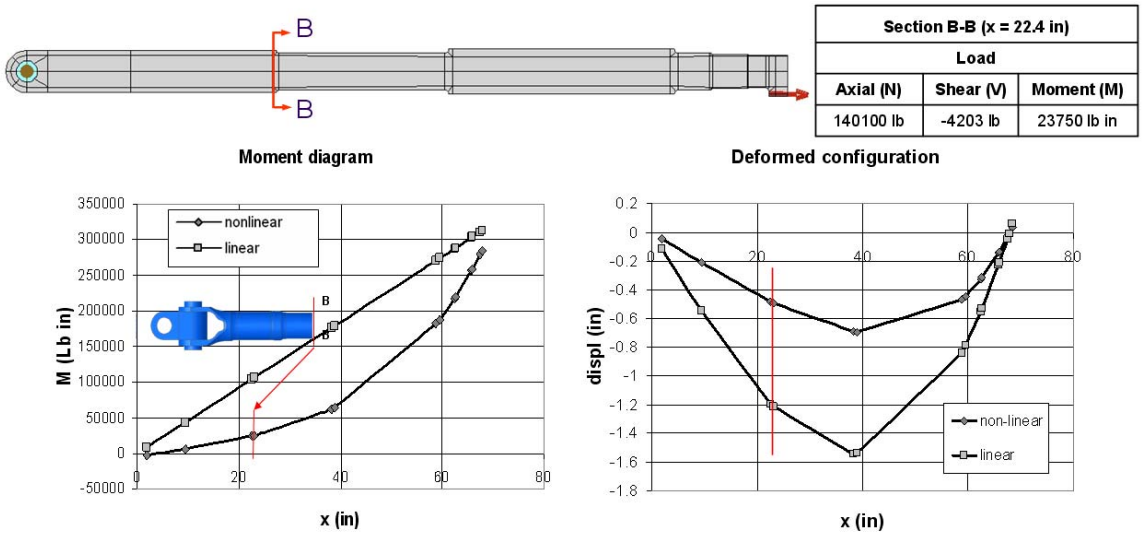

Section B-B (x = 22.4 in)		
Load		
Axial (N)	Shear (V)	Moment (M)
140100 lb	-4203 lb	23750 lb in

Figure 5: Moment diagram and deformed configuration for the arrestment load case.

Since the moment variation is nearly linear from the center of the fastener to Section B-B, it was assumed that the stress distribution in the region of interest could be determined by solving a local 3-D contact problem of the shank. The solution for the local 3-D model was obtained using as loads the moment, shear and axial forces computed from the 2-D solution at Section B-B (Figure 6). These loads were applied as distributed tractions and the local model included the nonlinear effect of contact between the pivot and arm assemblies. Since the loads obtained from the 2-D nonlinear solution were computed from the deformed configuration, and the local 3-D contact solution considers the undeformed configuration, the shear force was adjusted so that the net moment at the center hole of the pivot was zero. This was expected to introduce no significant changes in the magnitude and distribution of the stresses in the region of interest, since the shear force obtained from the 2-D geometric nonlinear analysis (-4203 lb) is a small fraction (3%) of the applied axial load (140100 lb).

COPY

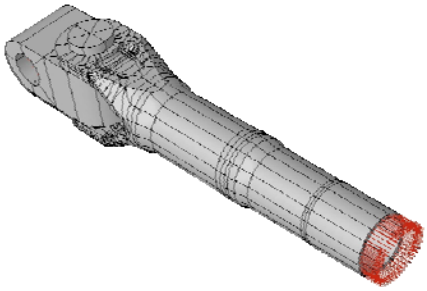

Figure 6: 3-D Local model of the shank with loads applied at section B-B.

As is shown in Figure 6, the moment (23750 lb-in), adjusted shear force (-1060 lb) and normal force (140100 lb) at Section B-B have been converted into the equivalent traction distributions over the circular cross section. To enforce equilibrium conditions, a sinusoidal bearing load of axial resultant 140100 lb was assigned to the bore of the pivot. Contact zones were specified between the pin and clevis of the shank, and between clevis and pivot. A contact solution was performed, and the stress distribution in the region of interest was extracted. Figure 7 shows the maximum first principal stress ($\sigma_{1\max}$) in the inner bore of the shank while Figure 8 shows the $\sigma_{1\max}$ on the outer surface of the shank in the region of interest.

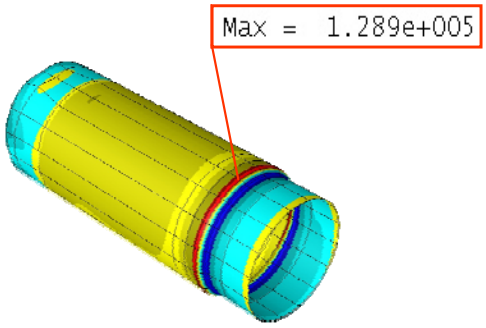

Figure 7: Value of $\sigma_{1\max}$ in the inner bore of the region of interest for the local contact model.

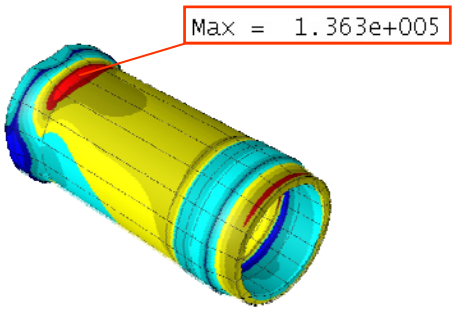

Figure 8: Value of $\sigma_{1\max}$ in region of interest for the local contact model.

COPY

COPY

Two more cases were considered for the local model to determine whether the complexity of the model could be reduced without significantly affecting the stress distribution in the region of interest. The second model involved the removal of contact considerations in favor of distributed springs at the clevis (Figure 9). In doing so, the model complexity was significantly reduced as it is no longer a nonlinear problem due to the contact. The goal was to determine if the effect of this additional modeling reduction was significant on the inner bore $\sigma_{1\max}$. As can be seen in Figures 10 and 11, the effect is not significant and therefore the simpler model without contact could also be used for the local analysis.

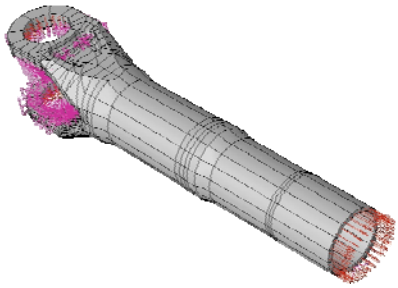

Figure 9: 3-D local model without contact.

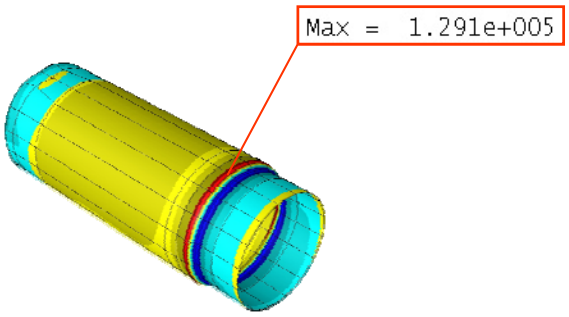

Figure 10: Value of $\sigma_{1\max}$ in the inner bore region for the local model without contact.

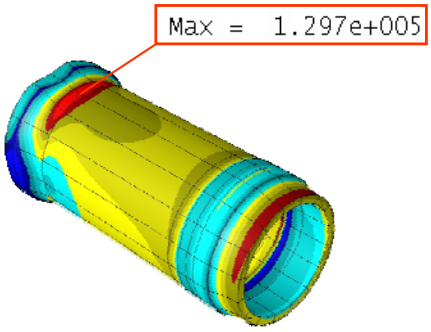

Figure 11: Value of $\sigma_{1\max}$ in the region of interest for the local model without contact.

COPY

One more simplification of the local model was considered, consisting of the removal of the entire clevis portion of the model in favor of distributed springs at the cross-section. Again, the goal was to compare the results with those obtained for the local contact model to determine the effect on the stress distribution in the region of interest. As can be seen in Figure 12, the influence of the simplification does not affect the value of $\sigma_{1\max}$ substantially.

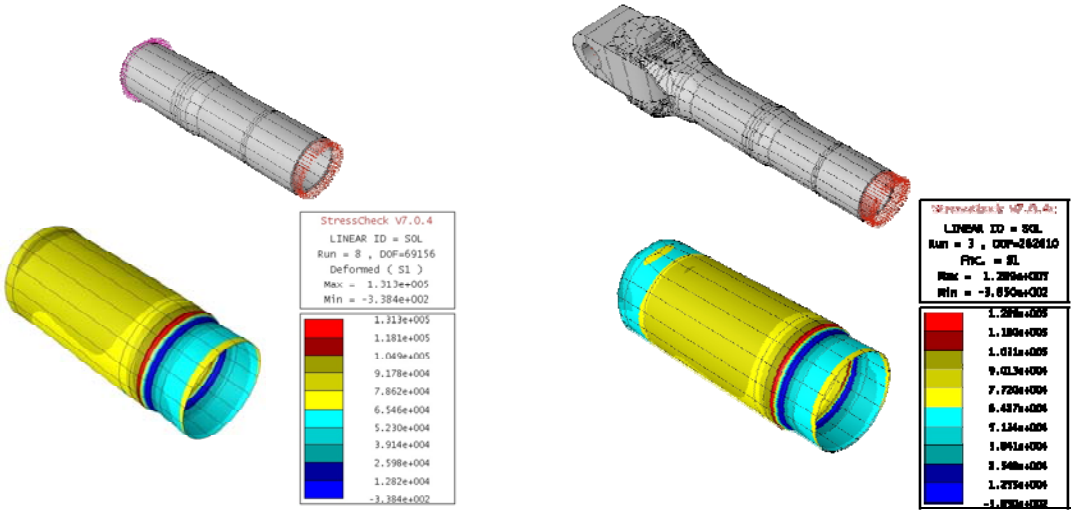

Figure 12: Comparison of $\sigma_{1\max}$ in the inner bore: Contact model (right) and simplified model (left).

In summary, it is shown that for the arrestment load case, the local contact model and the two local models without contact will give an approximation for the axial stress distribution (in the region of interest) very close to one another.

3) Modeling of Case 2: Hook Bounce Load

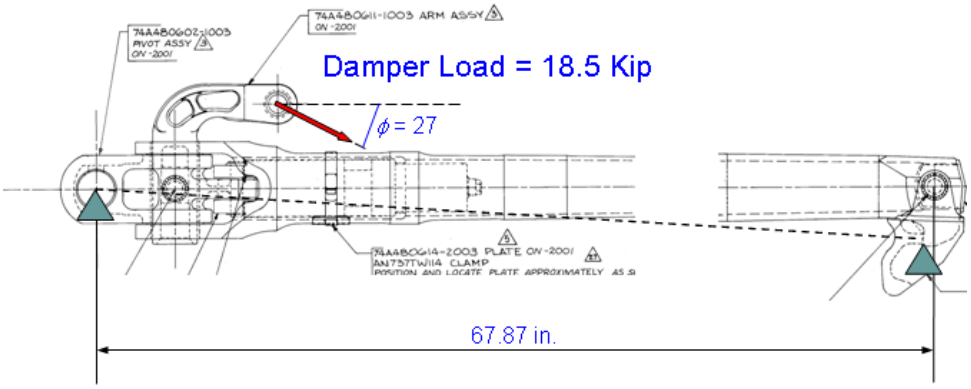

Figure 13: Hook bounce load case configuration.

3.1) Modeling Approach and Results

In the hook bounce load case an 18.5 kip damper load is applied to the pivot arm at a 27 degree angle to the horizontal as shown in Figure 13. The modeling approach for the hook bounce load case was very similar to the arrestment load case. A 2-D model of the complete shank was used to determine the resultants at Section B-B and these loads were applied as traction distributions in a 3-D local model of the clevis end. To simulate the forces and moments generated at the arm assembly, a set of equivalent traction distributions were applied at section B-B. A vertical traction was then introduced at the hook end to represent a simply-supported reaction condition, and a fastener element was used to simulate the contact between assemblies. The 2-D model for the hook bounce load case is shown in Figure 14. The resultant moment and shear force at section B-B are shown in Table 1. As expected, the moment at Section B-B is far more dominant in the hook bounce load case than for the arrestment load case (92700 lb-in versus 23750 lb-in, respectively).

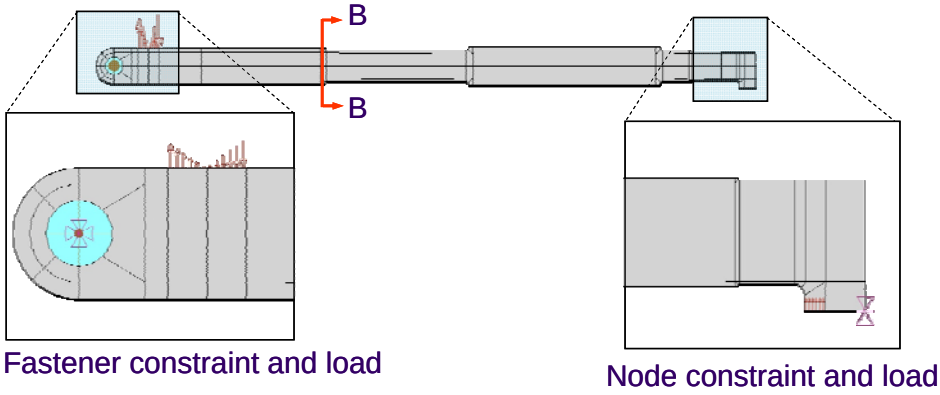

Figure 14: 2-D model for the hook bounce load case.

Table 4: Resultant moment and shear force at section B-B for the hook bounce load case

Section B-B (x = 22.4 in)		
Load		
Axial (N)	Shear (V)	Moment (M)
0 lb	2016 lb	92700 lb in

Similar to the modeling approach used in the arrestment load case, the loads given in Table 4 were converted to equivalent tractions and applied to 3-D local models at Section B-B. The most complex of the 3-D local models included contact at the clevis end between the pivot, damper arm, and clevis (Figure 15). The least complex of the 3-D localized models did not consider contact or the clevis geometry as distributed springs were used to model the stiffness at the clevis end (Figure 16). Again, the goal was to determine if the simplified local model could accurately

capture the inner bore $\sigma_{1\max}$ given by the local model with contact. Comparing Figures 17 and 18, both cases give practically the same value for $\sigma_{1\max}$ (108 ksi). It will also be shown in the Validation section, that the axial strains given by the model are strongly correlated with available experimental strain information.

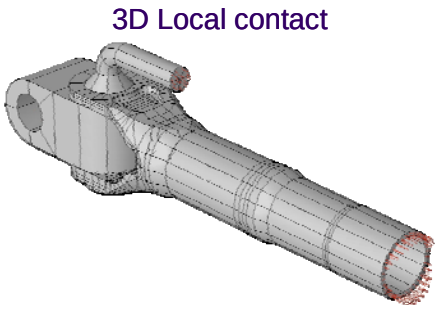

Figure 15: 3-D Local model with contact for the hook bounce load case.

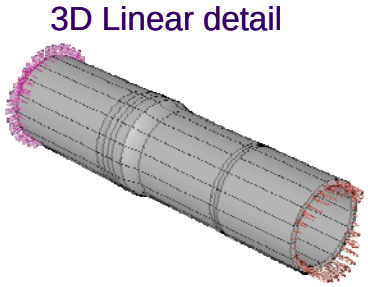

Figure 16: Simplified 3-D local model for the hook bounce load case.

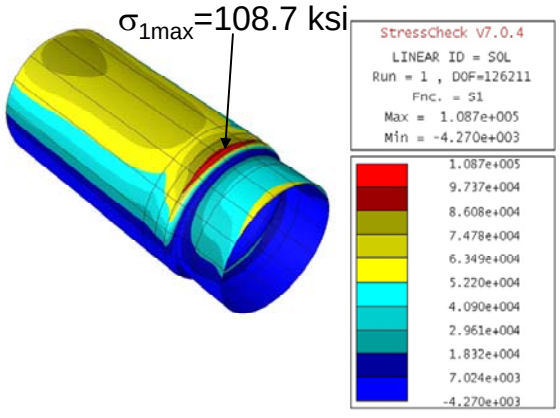

Figure 17: Extraction of $\sigma_{1\max}$ in the inner bore region for the local contact model.

COPY

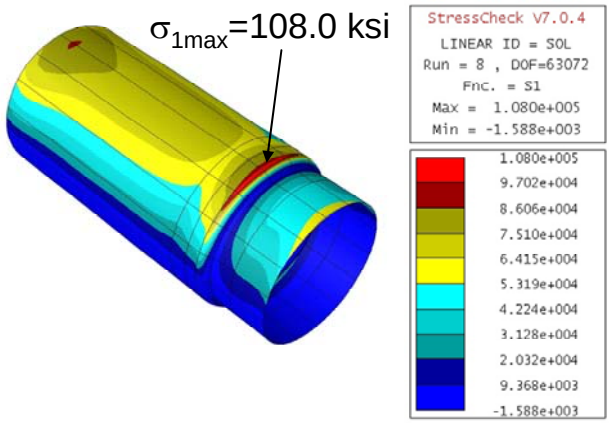

Figure 18: Extraction of $\sigma_{1\max}$ in the inner bore region for the simplified local model.

4) Validation: Comparison of StressCheck results with experimental strain surveys

Validation involves one or more metrics and corresponding criteria. In this case the metrics are the strain gage readings at certain location within the region of primary interest (Fig. 19). The criteria should be understood as criteria for rejection. Formulation of the criteria depends on the intended use of the model and the accuracy required. The model is rejected if any one of the criteria is not met. Setting the criteria properly for a validation experiment is very important. If the criteria are overly stringent then a valid model may be rejected. If the criteria allow large differences between the predicted and measured metrics then invalid models may not be rejected. In this case the criteria were based on the estimated repeatability of experimental data. Specifically

1. In regions of shallow strain gradients, differences between measured and predicted strains must be 5% or less.
2. In regions of large strain gradients, differences between measured and predicted strains can be larger than in item 1 above, and are to be evaluated on a case-by-case basis. The intent is to estimate the repeatability of strain measurements.

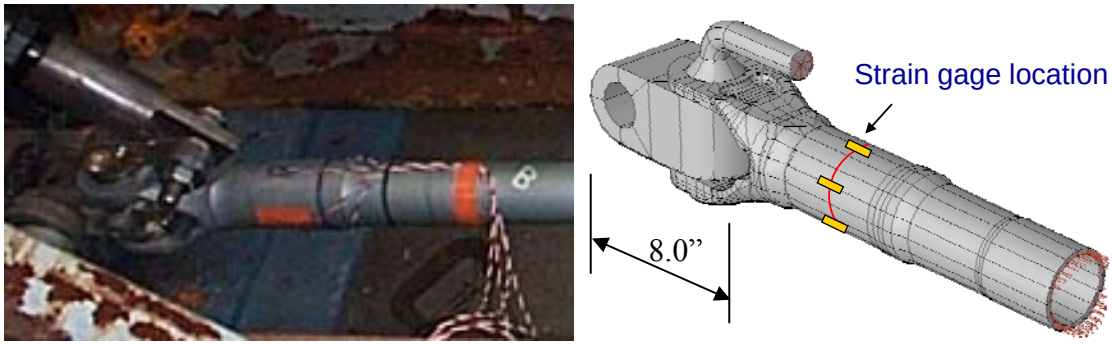

Figure 19: Strain Gage Locations

COPY

COPY

4.1) Hook Bounce Load Case Validation

For the hook bounce load case, the numerical predictions based on the 3-D local model shown in Figure 19 compared well against available experimental results (Figure 20). These results give confidence that the mathematical model used for representing the hook bounce load meets criterion 1.

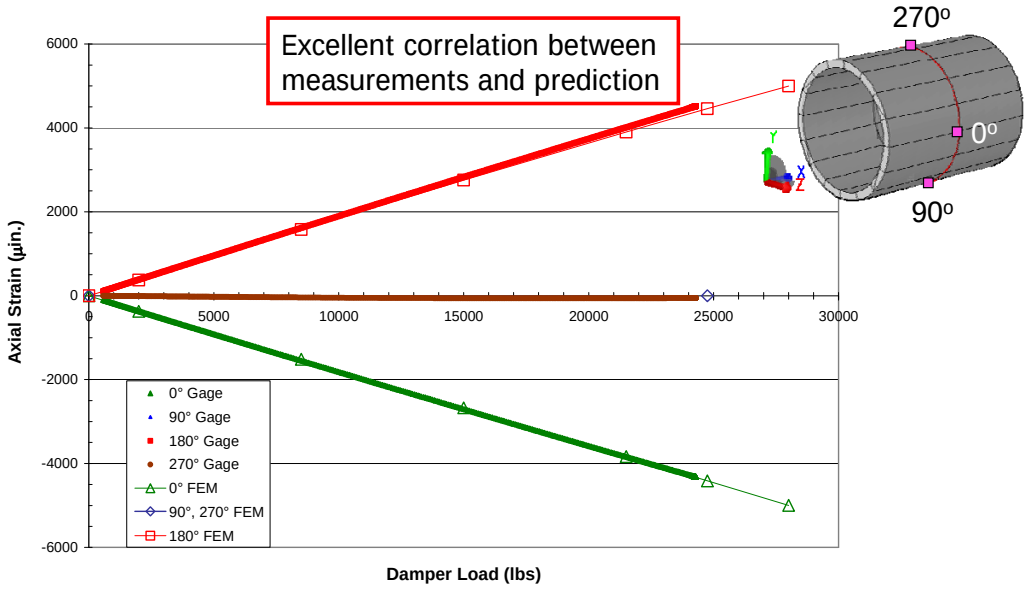

Figure 20: Model validation - Comparison of predicted and measured axial strains at 4 locations for several values of the hook bounce (damper) load.

For example, at a compressive damper load of -24293 lb, the average strain gage reading for the 0 deg. gage was -4312 □, while the FEM prediction was -4331 □ (a difference of only 0.44%). The strain gage readings for the maximum test load (-24293 lb) and the comparison with the predictions are summarized in Table 5.

Table 5: Strain gage readings and FEM predictions at two locations for a damper load of -24293 lb

Condition	Strain [□in/in]	
	0° gage	180° gage
Run #1 reading	-4318	4518
Run #2 reading	-4312	4512
Run #3 reading	-4306	4512
Average	-4312	4514
FEM Result	-4331	4381
(FEM-Avg)/Avg *100	0.44%	-2.95%

COPY

COPY

4.2) Arrestment Load Case Validation

For the arrestment load case, the numerical predictions of the axial strains given by the 3-D local model shown in Figure 21 and the strain gage survey at 8 circumferential locations for an arrestment axial load of 137 kip are shown in Figure 22. There is substantial difference between predicted and experimental strain values for the locations in the upped half of the shank, with a maximum difference of 19% for the strain gage located at the top. Therefore, based on the stated criteria, the model has to be rejected.

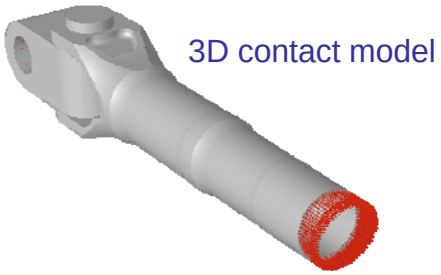

Figure 21: Arrestment load case 3-D local contact model.

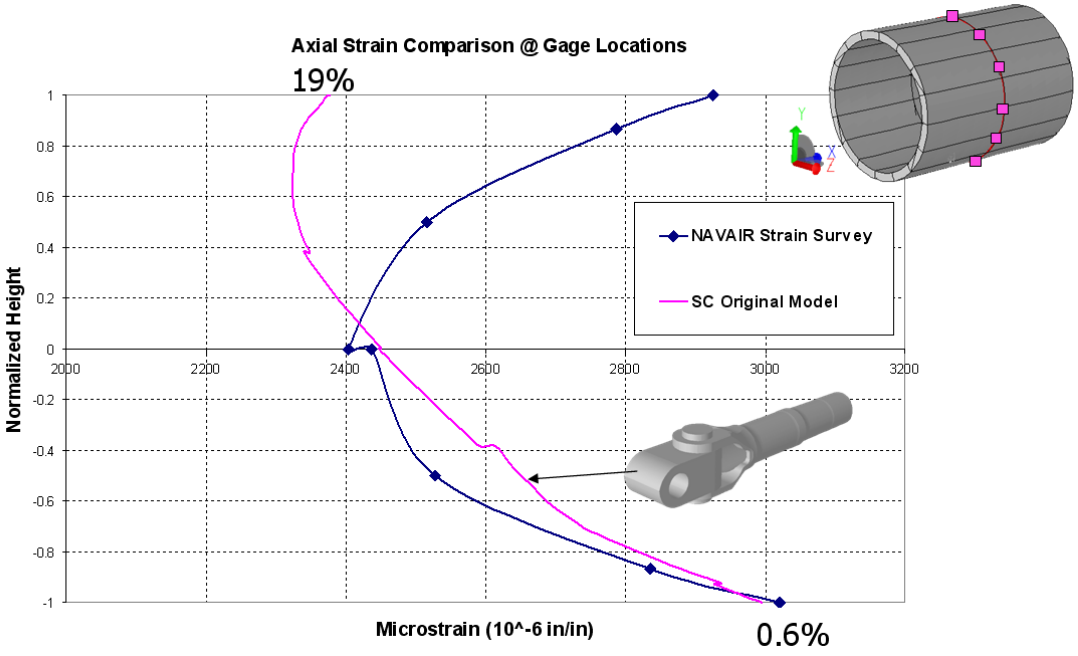

Figure 22: Validation of Arrestment Load Case (3-D local contact model). Axial Strains for 137 kip axial load.

The model was reevaluated to determine the reason for rejection. A modification to the original modeling approach was investigated as described in the following.

COPY

5) Updated Model: Full Arrestment Hook with Geometric Nonlinearities

The evaluation of the modeling strategy indicated that the combination of a 2-D geometric nonlinear model with a 3-D local contact model was responsible for the observed difference between prediction and experiments. Because the bending moment computed from the 2-D model, from Section B-B to the pinned connection, decreased to zero linearly, it was assumed that the shear at section B-B of the local 3-D contact model could be adjusted proportionally to equilibrate the moment (Figure 5). This implied that a linear model, albeit with boundary conditions resulting from a geometric nonlinear analysis, was sufficient to represent the behavior of the shank from Section B-B to the pinned connection. However, at the axial location of the strain gages the magnitudes of the axial strains were not consistent with prediction, with significant underestimations occurring at the top of the shank (Figure 22). Therefore, this linear model does not adequately capture the axial strain distribution between Section B-B and the pinned connection given this loading condition due to the strong coupling between bending and membrane strains.

To overcome this problem, the full tail hook must be modeled and solved incorporating both contact and geometric nonlinear analysis. Because geometric nonlinear analysis with contact is outside the current capabilities of StressCheck, a simplified approach was considered. A full 3-D model of the tail hook assembly was created with the components in the contact region "fused" together (all elements connected), and a geometric nonlinear analysis performed for the arrestment load case. The updated StressCheck arrestment hook model is shown in Figure 23. The elements of the gold-colored region are fused to the clevis bore, and a 137 kip axial load was applied to the element faces at the hook end as shown in the figure.

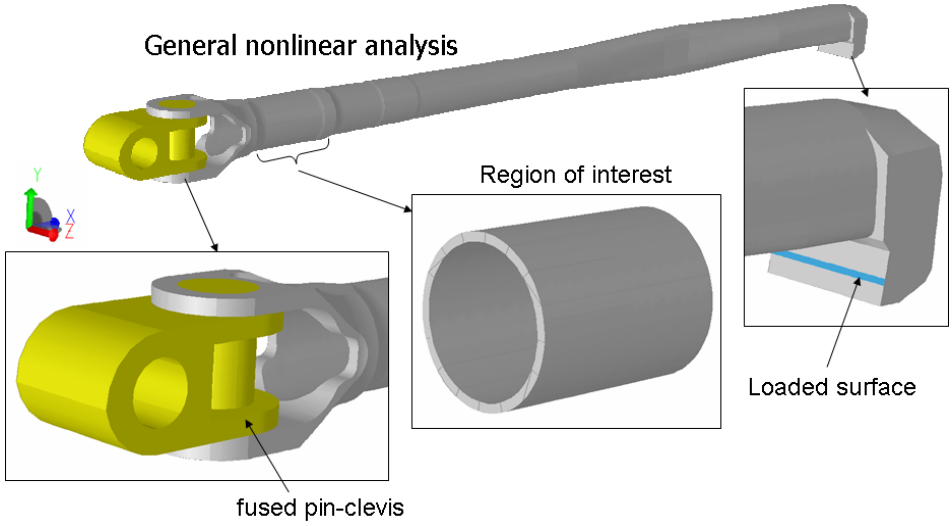

Figure 23: Full 3-D arrestment hook model with fused pin-clevis.

The solution to the updated model, which included geometric nonlinear effects, was compared to the previous solutions for the arrestment load case (Figure 24). Observe that the incorporation of the geometric nonlinear effects (light blue curve) improved the overall shape of the axial strain distribution when compared to the strain survey results. For example, at the bottom surface the strain gage measurement was 3017 □in/in while the FEM prediction was 2940 □in/in (a difference of 2.6%), and at the top surface the strain gage measurements was 2922 □in/in while the FEM prediction was 2570 □in/in (a difference of 12%). These are regions of high stress gradient through the shank thickness and therefore the second criterion is applicable. Also superimposed in the graph are the predicted strains from the 3-D local contact model in which the bending moment was removed and only the axial load was applied at section B-B (green curve). This was studied as a limiting case in order to show the influence of bending in the strains values at the survey location. The results for the top, bottom and center locations are summarized in table 6, where the % difference between the average strain gage reading and the prediction of a particular model is shown bracketed next to the prediction. The % difference is computed as (Avg. reading - prediction)/Avg. reading x 100.

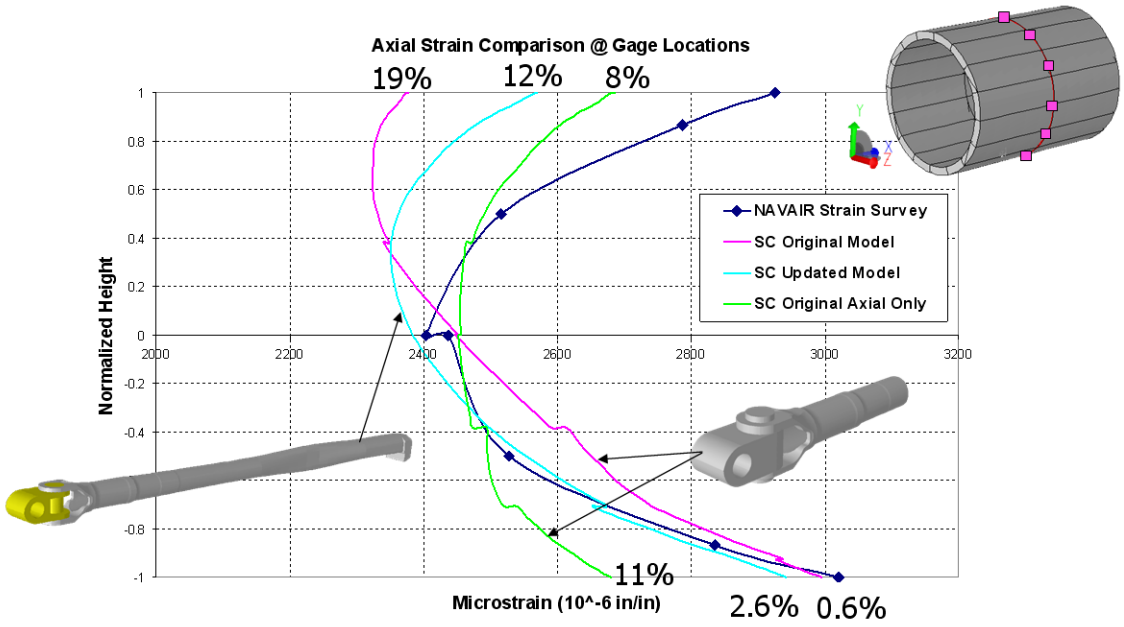

Figure 24: Comparison of predicted axial strains and strain survey results (axial load of 137 kip).

When comparing the axial stress distributions in the region of primary interest of the updated model with the original 3-D local contact model, it can be seen that there is a small difference in both the distribution of the stress and the magnitudes (Figure 25). Therefore, though the maximum predicted axial strains on the outer surface of the shank are quite different for both models, the magnitude and distribution of axial stresses in the inner bore are not as sensitive to the modeling assumption (less than 1% difference).

Table 6: Strain gage reading and FEM predictions at three locations. Arrestment load case (137 kips)

Condition	Strain [□ in/in]			
	Top	Center 1	Center 2	Bottom
Run #1 reading	2922	2432	2400	3013
Run #2 reading	2921	2430	2400	3018
Run #3 reading	2922	2429	2400	3019
Average	2922	2430	2400	3017
FEM original	2380 (19%)	2450 (-0.8%)	2450 (-2.1%)	3000 (0.6%)
FEM original - Axial only	2690 (8%)	2460 (-1.2%)	2460 (-2.5%)	2680 (11%)
FEM modified	2570 (12%)	2380 (2.1%)	2380 (0.8%)	2940 (2.6%)

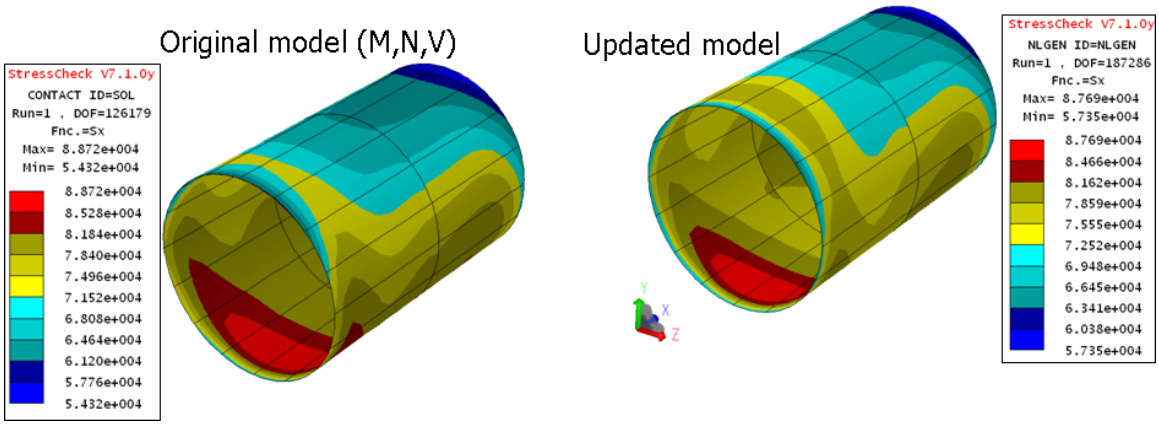

Figure 25: Inner bore axial stress distribution for the original and updated models.

Finally, Figure 26 shows convergence information in the region of primary interest. The general nonlinear solution of the full 3-D model of the assembly was obtained for p-levels 5, 6, and 7, and the axial strain distribution along a circumference and maximum axial stress $\square_x$ inside the bore of the region of interest were extracted for all three runs. Figure 26(a) shows the strain distribution along a circle on the outer surface of the shank (at the strain gage location) for all three runs. The results indicate a strong convergence of the strain for all the points. Figure 26(b) shows the convergence of the maximum axial stress at the inner bore of the shank in the region of interest as a function of the number of degrees of freedom (DOF). The estimated maximum for $\square_x$ differs only by 0.14% with the value computed from the finite element solution corresponding to run #3 (p=7).

COPY

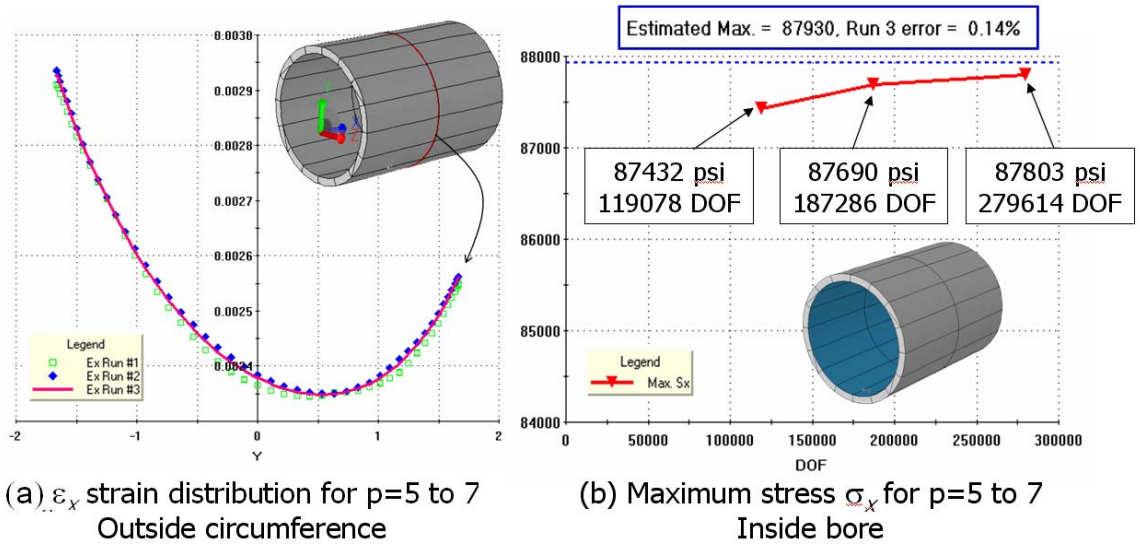

(a) ε_x strain distribution for p=5 to 7 Outside circumference

(b) Maximum stress σ_x for p=5 to 7 Inside bore

Figure 26: Convergence information for the updated 3-D model. (a) Axial strain on the outside surface for 3 FEA runs; (b) maximum axial stress in the inner bore for 3 FEA runs.

6) Summary

Verification and validation (V&V) procedures were used to evaluate the effect of modeling considerations on the axial stress distributions in the region of primary interest of the arresting hook for two load cases. Verification was accomplished by p-extension, that is, by increasing the number of degrees of freedom while keeping the mesh fixed and checking that the quantities of interests (strain and stresses) were practically independent of the discretization parameters (mesh and polynomial order of the elements). For both load cases, the modeling approach consisted of solving a global 3-D model including contact and geometric nonlinearities, extracting stress resultants and applying them to a local 3-D contact model that did not include large deformations. The validation task consisted of comparing the predicted strains at specific locations with experimental results. It was found that while for the hook bounce load case the agreement between predicted and experimental strains was very good (within the requirements of the first criterion), the discrepancy for the arrestment load case was not acceptable.

The model for the arrestment load case was revised and modified by solving a complete 3-D tail hook assembly accounting for geometric nonlinearities but ignoring the effect of contact. With the modified model the comparison between predicted and measured strains were much closer than previously and considered to have satisfied the second criterion because the strain survey area is located in a high strain gradient region. It must be noted also that while the axial strains were not as close as in the case of the bounce load, the shank inner bore axial stresses in the region of interest were very insensitive to the modeling assumptions.

COPY

The writers believe that correlation between experiment and prediction could be further improved for the arrestment load case if geometrical nonlinearities and mechanical contact could be represented in the mathematical model. The current implementation of StressCheck does not support that capability, however. It is expected that this limitation will be removed in a future version of StressCheck. Nevertheless, within the accuracy range considered useful from the point of view of the intended use of the model, no reason was found to reject the simplified model described in this report.

THIS PAGE INTENTIONALLY LEFT BLANK

APPENDIX E
SHANK TEST FIXTURE

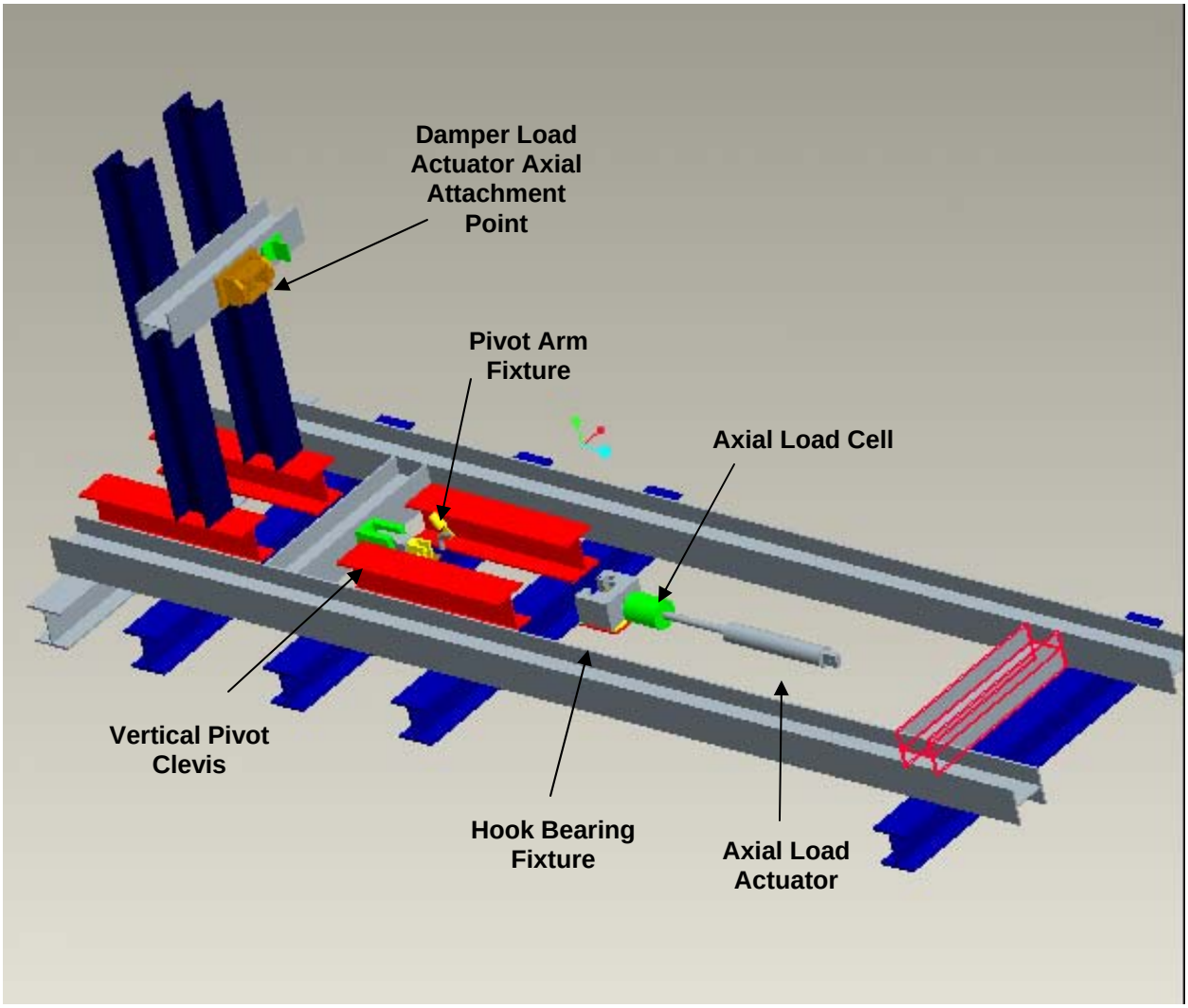

Figure E-1: General Shank Test Fixture Overview (Partial)

Figure E-2: Test Fixture Showing Damper Actuator

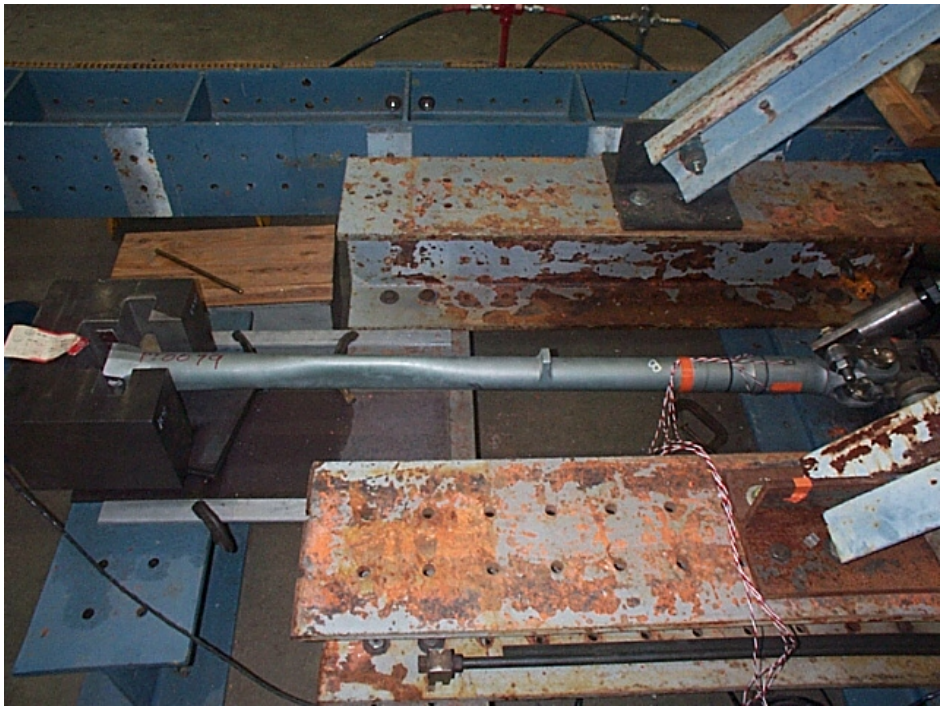

Figure E-3: Arresting Shank Installed in Test Fixture

Figure E-4: Hook End Fixture and Axial Load Cell

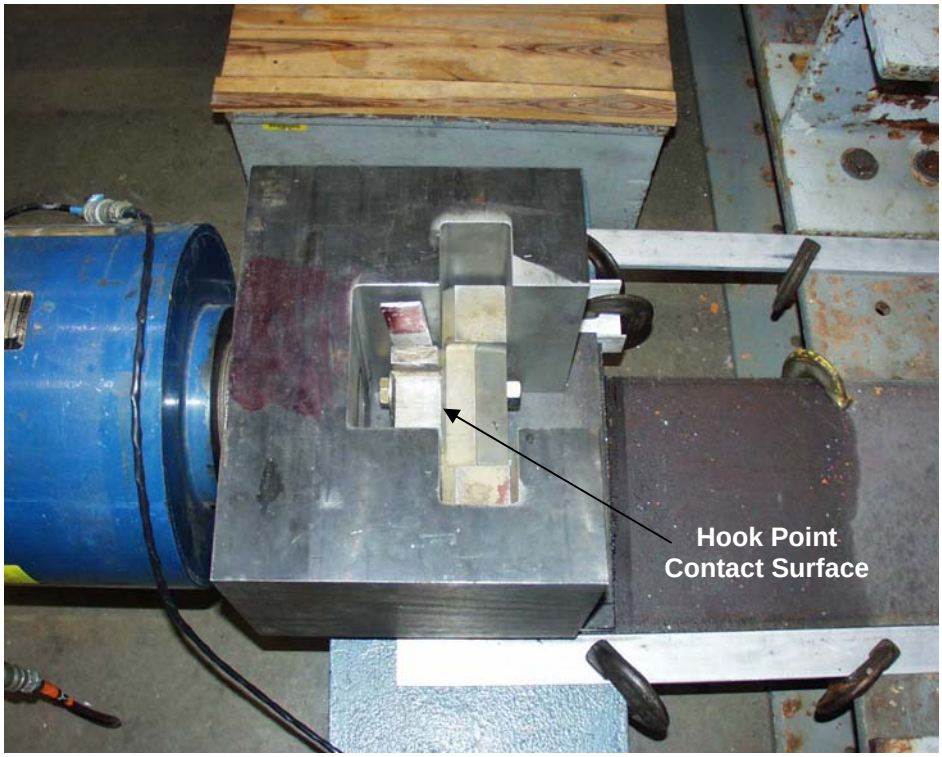

Figure E-5: Top View of Hook End Fixture

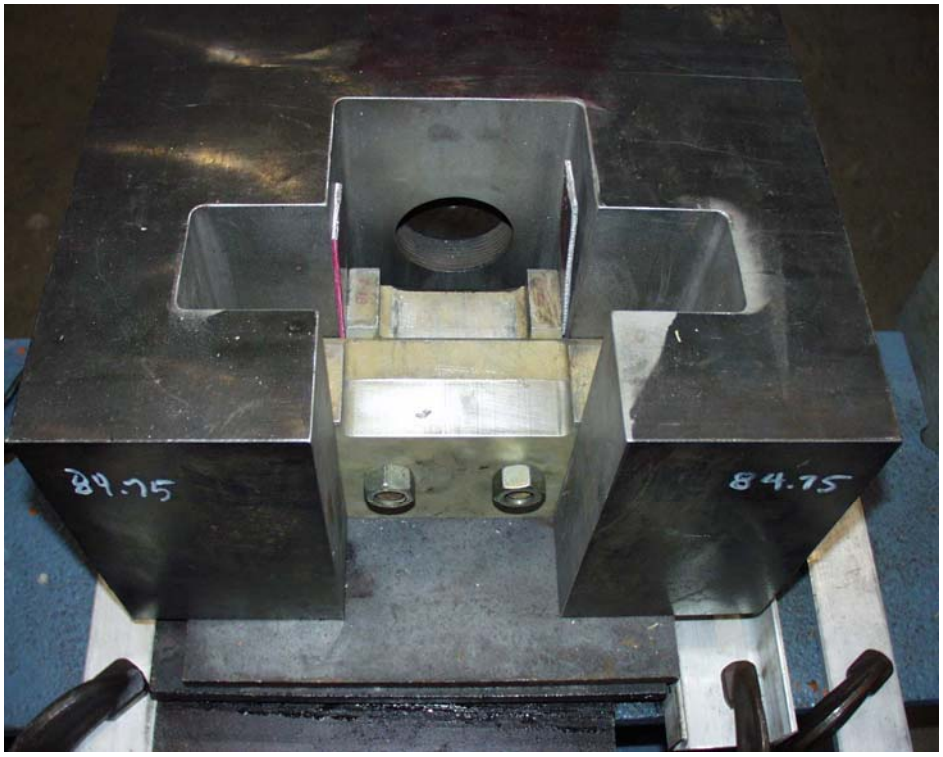

Figure E-6: Forward View of Hook End Fixture

APPENDIX F
FATIGUE FAILURE ANALYSIS

Figure F-1: Fatigue Test Failure Location for Shank PT0099 (Bottom View)

Figure F-2: Fatigue Test Failure Location for Shank PT0099 (Side View)

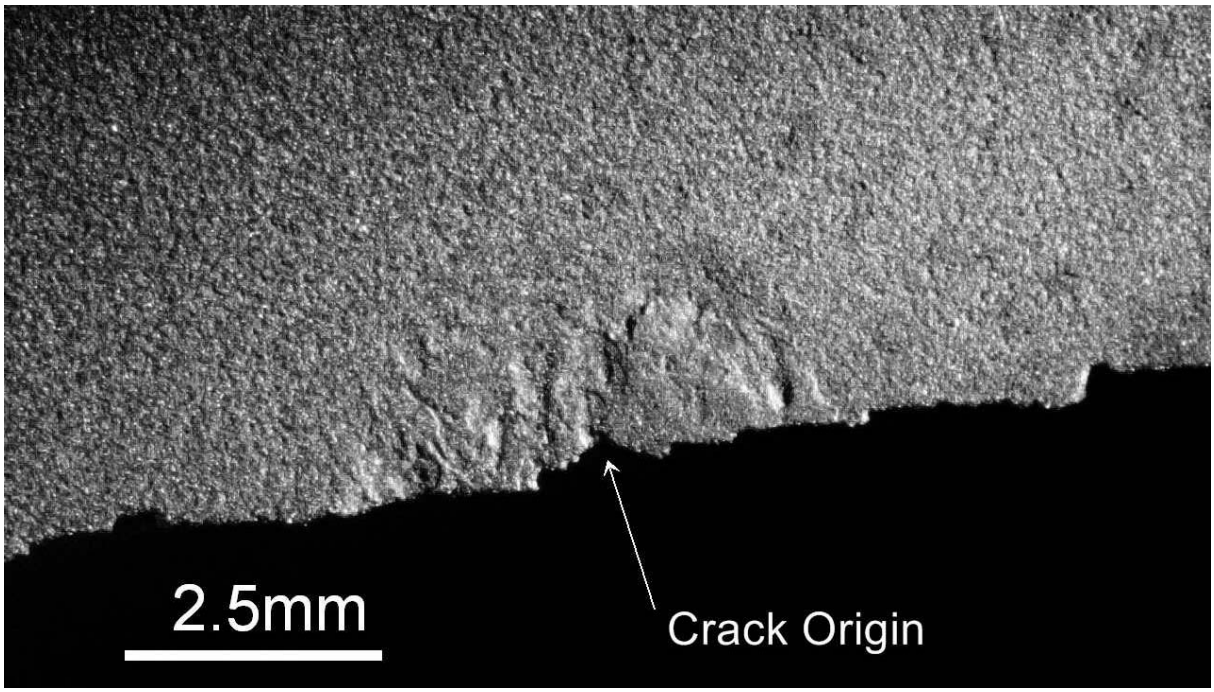

Figure F-3: Shank Surface View of Crack 1 Origin (PT0099)

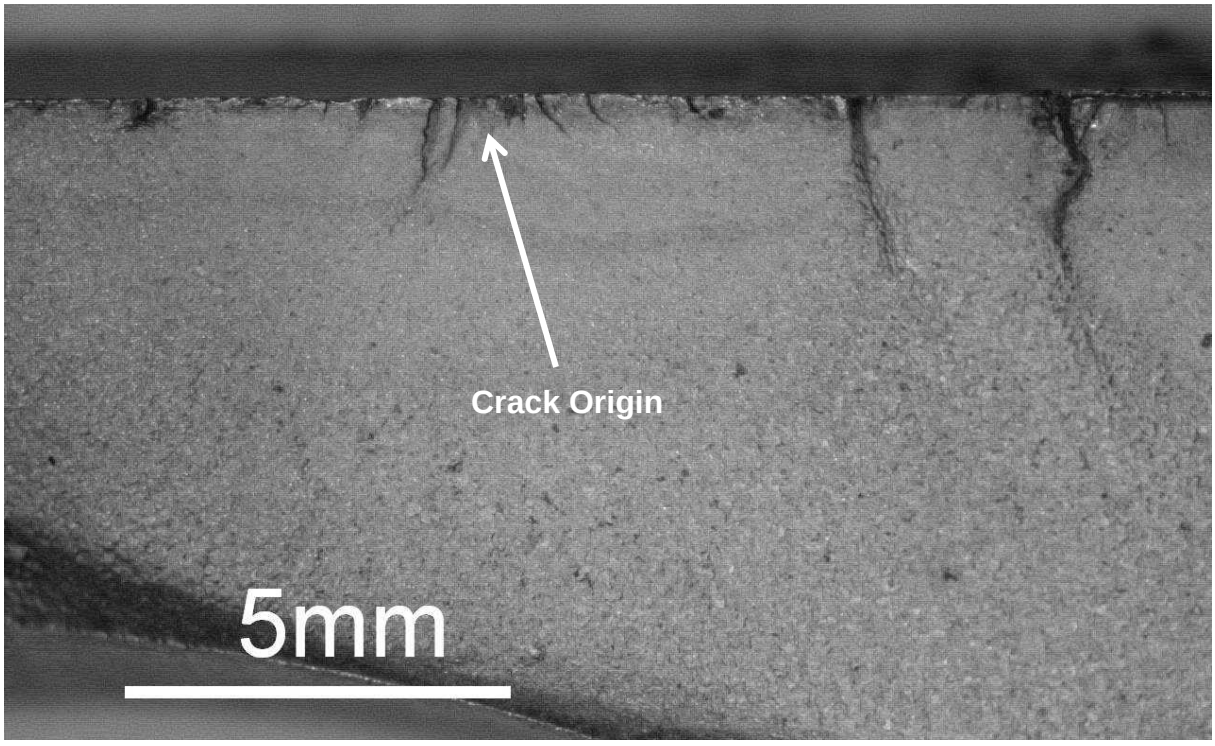

Figure F-4: Fracture Surface View of Crack 1 (PT0099)

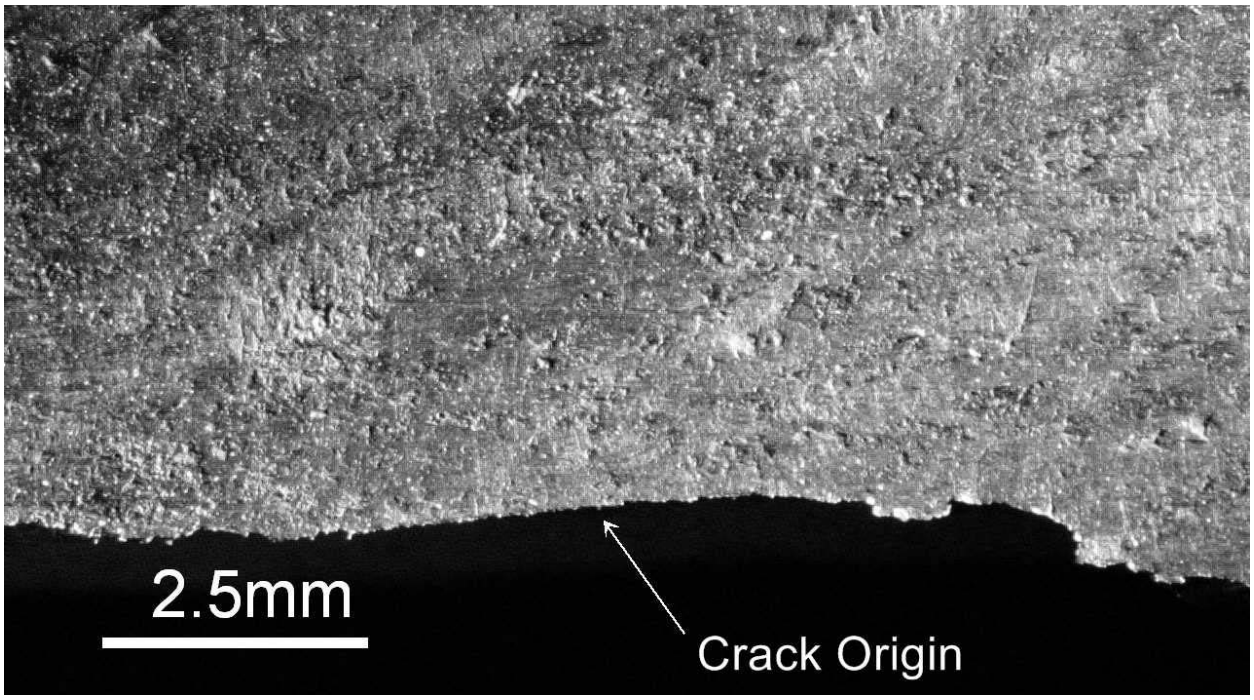

Figure F-5: Shank Surface View of Crack 2 Origin (PT0099)

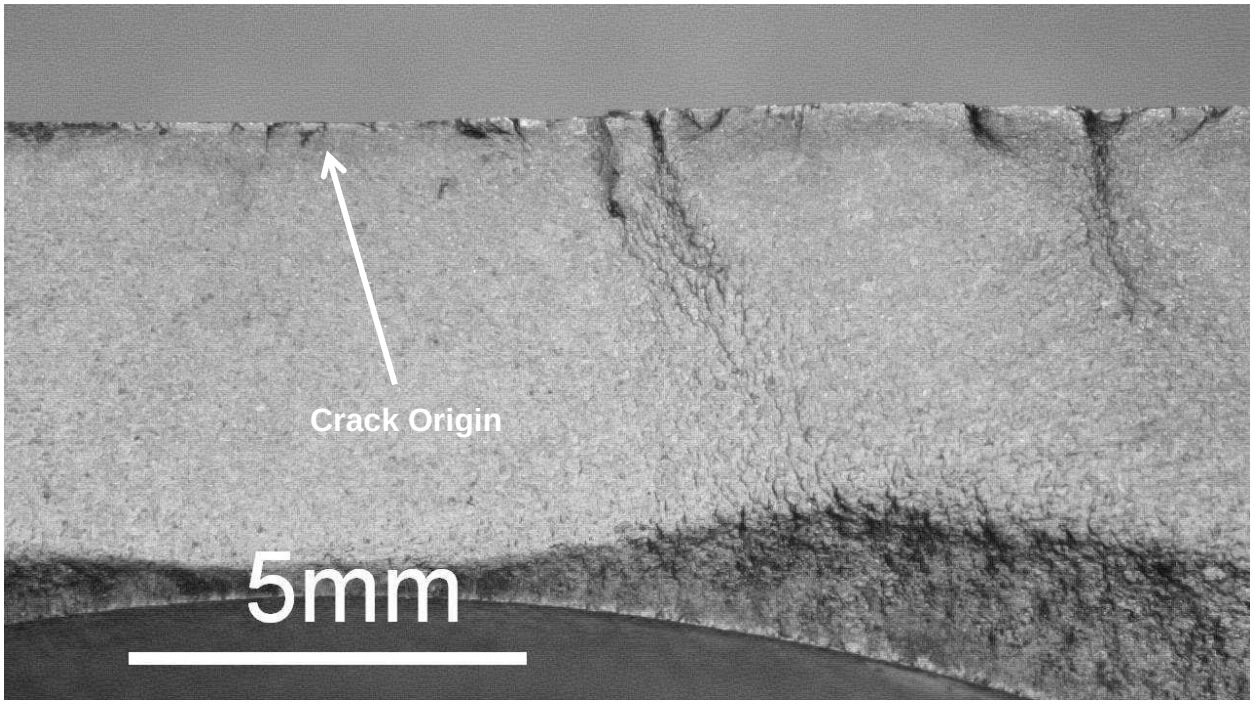

Figure F-6: Fracture Surface View of Crack 2 (PT0099)

Figure F-7: Fatigue Test Failure Location for Shank 0491 (Bottom View)

Figure F-8: Fatigue Test Failure Location for Shank 0491 (Side View)

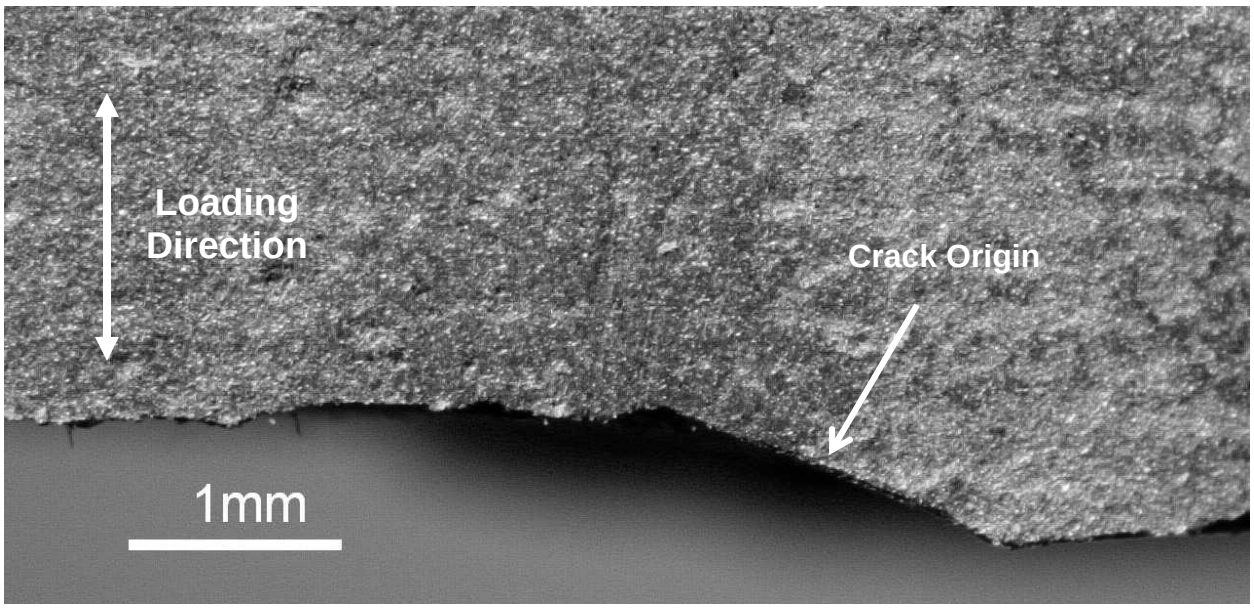

Figure F-9: Shank Surface View of Crack Origin (Shank 0491)

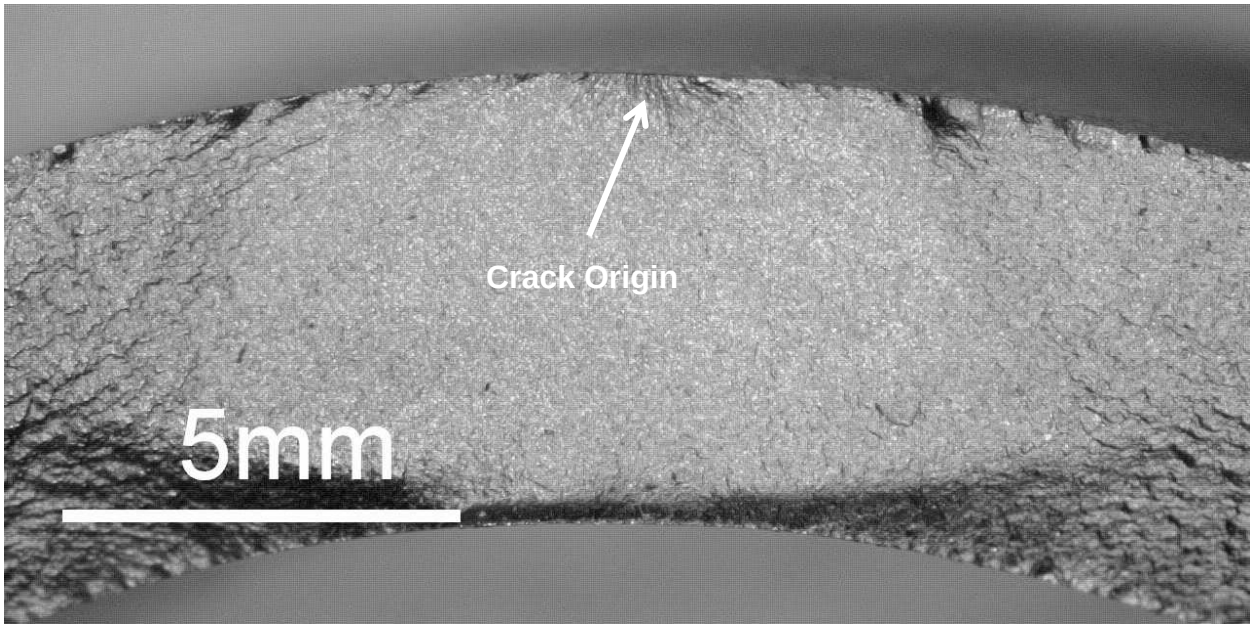

Figure F-10: Fracture Surface View of Crack Origin (Shank 0491)

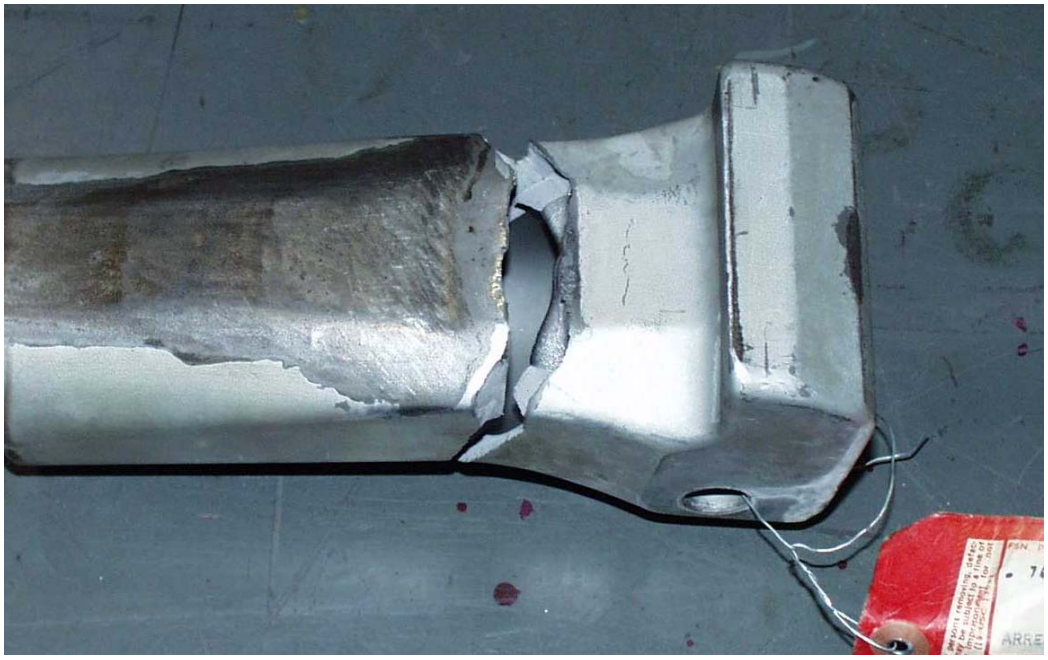

Figure F-11: Fatigue Test Failure Location for Shank PT0735 (Bottom View)

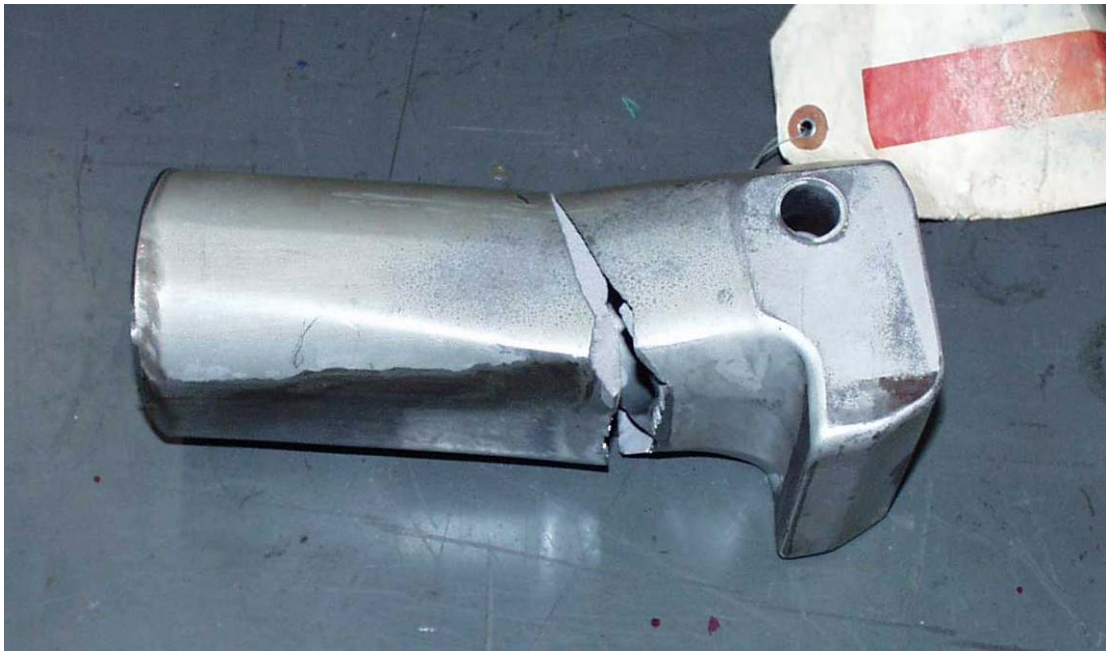

Figure F-12: Fatigue Test Failure Location for Shank PT0735 (Side View)

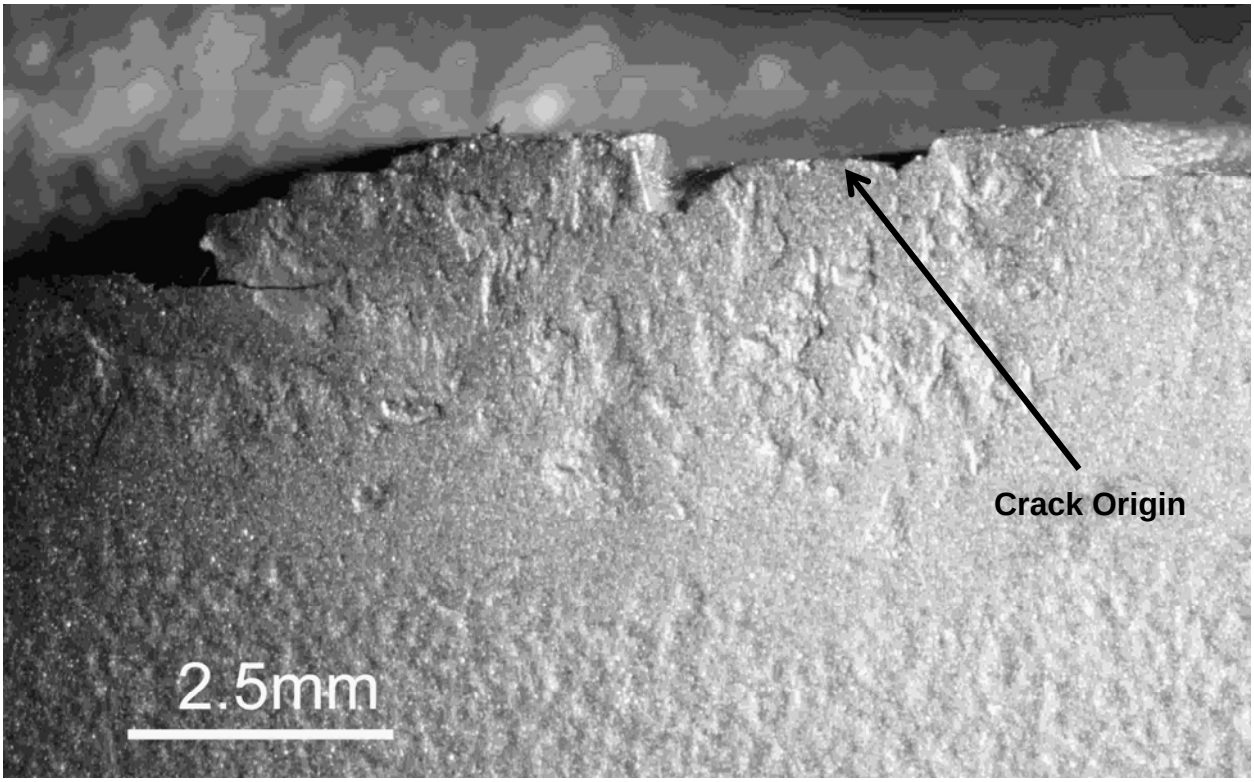

Figure F-13: Shank Surface View of Crack Origin (PT0735)

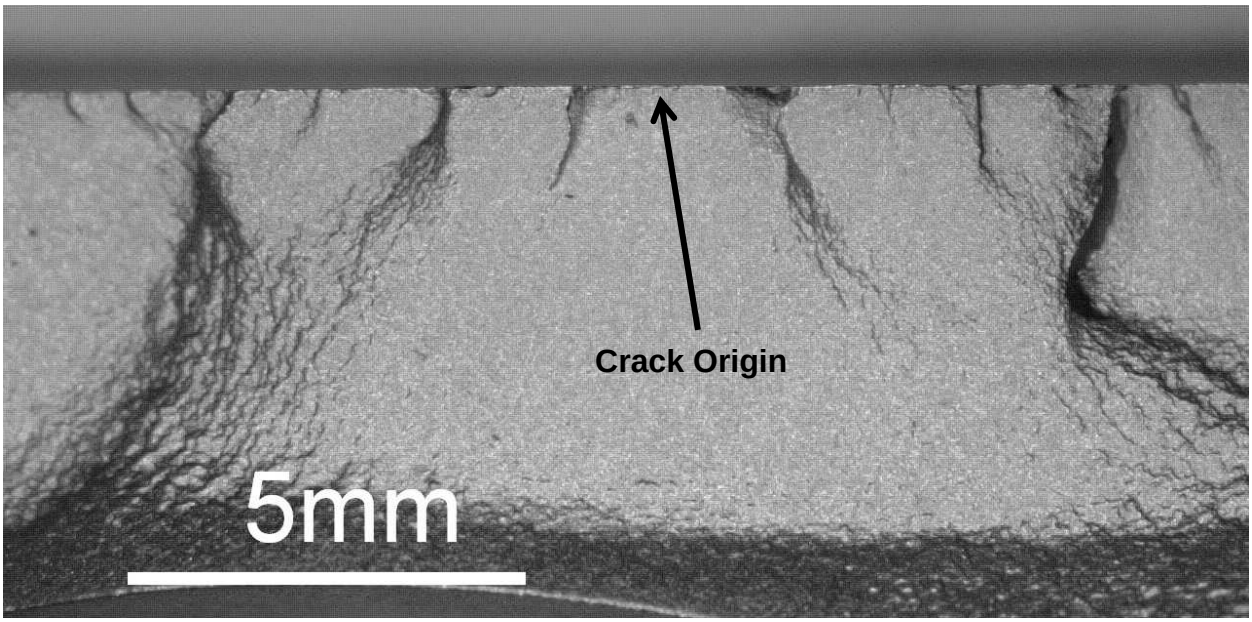

Figure F-14: Fracture Surface View of Crack Origin (PT0735)

Figure F-15: Section of Shank PT0099 with Noncritical Fatigue Cracks
(Forward of Lateral Damper Region)

Figure F-16: Section of Shank PT0099 with Noncritical Fatigue Cracks
(Forward of Lateral Damper Region)

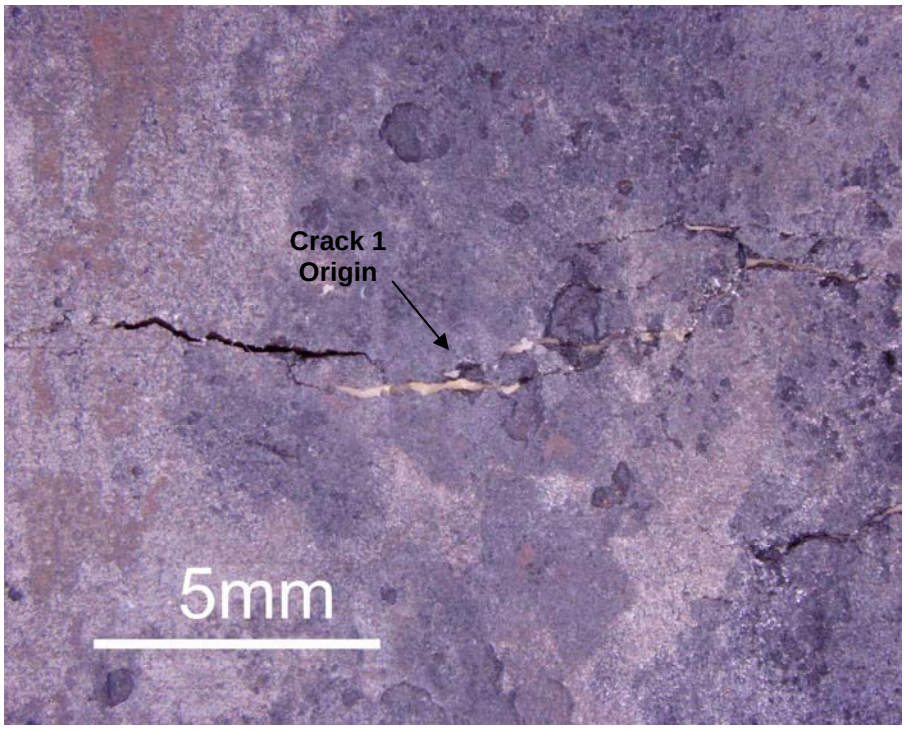

Figure F-17: Fatigue Crack on Corroded Inner Surface of Shank PT0099

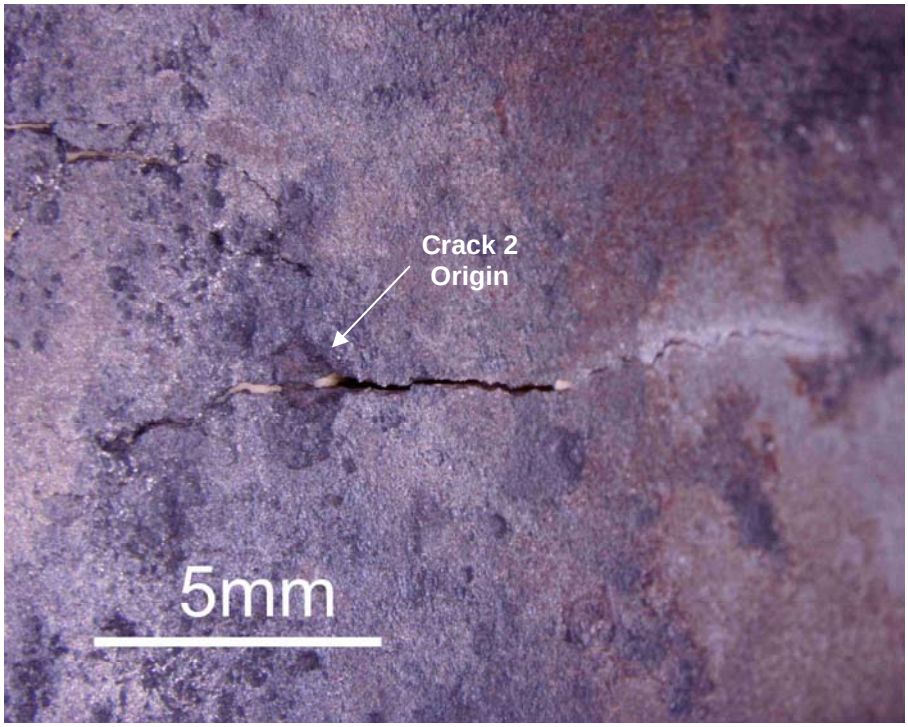

Figure F-18: Second Fatigue Crack on Corroded Inner Surface of Shank PT0099

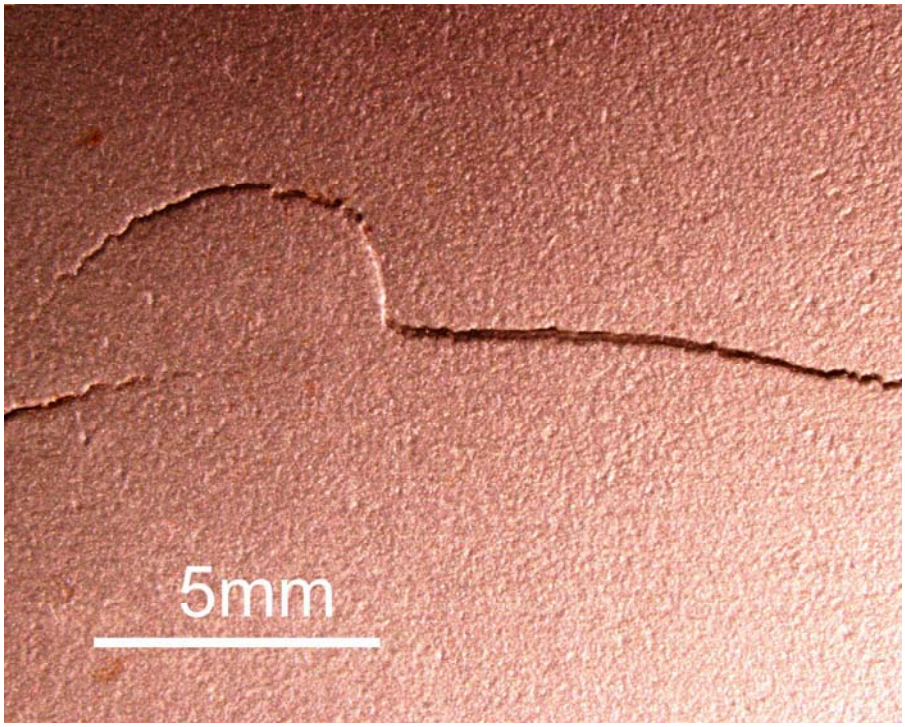

Figure F-19: Through-Crack on Outer Surface of Shank PT0099

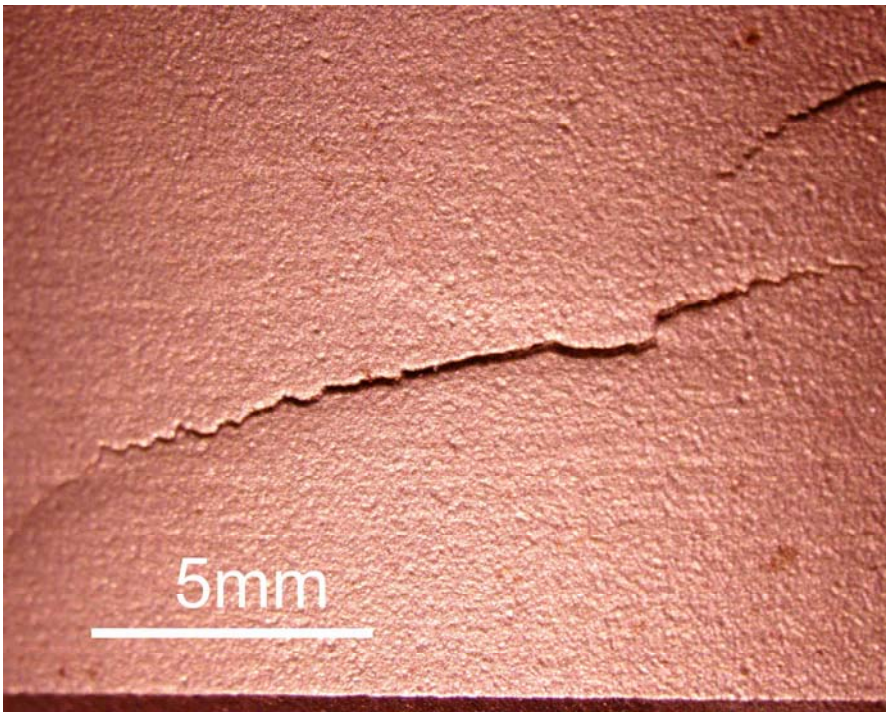

Figure F-20: Second Through-Crack on Outer Surface of Shank PT0099

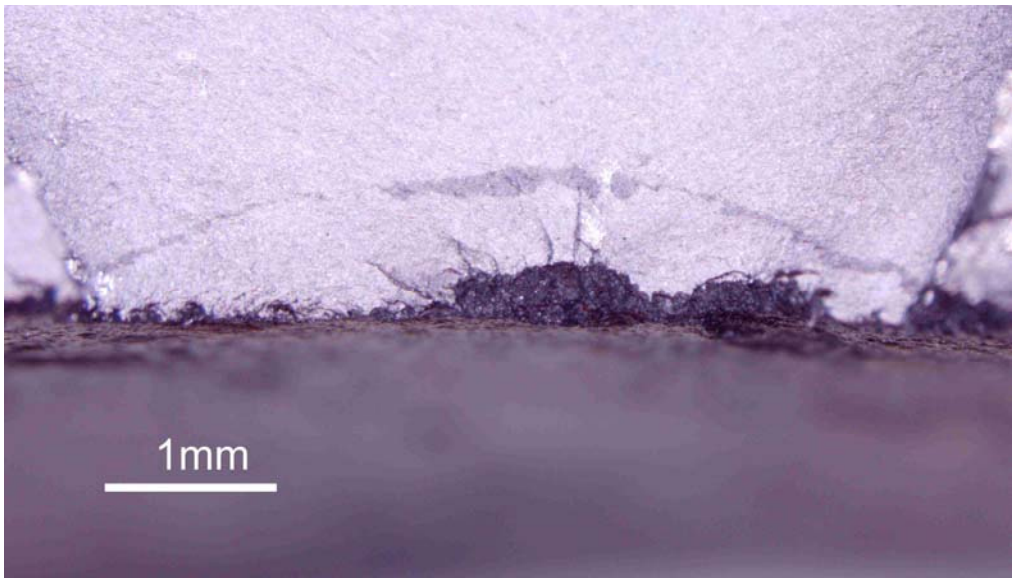

Figure F-21: Origin of Noncritical through Crack on Shank PT0099 (Crack 1)

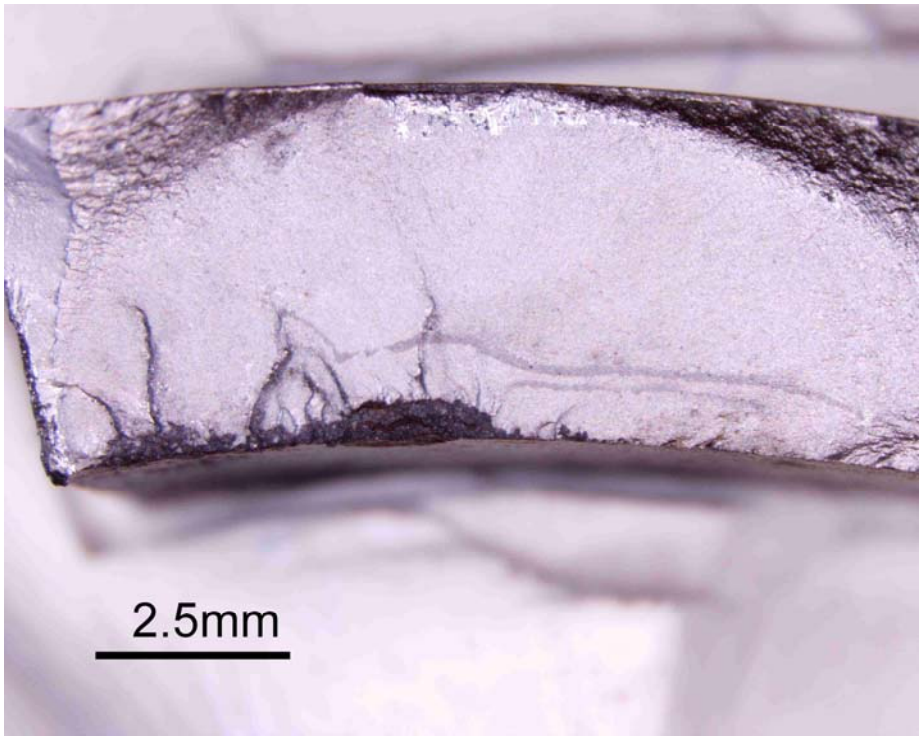

Figure F-22: Origin of Noncritical through Crack on Shank PT0099 (Crack 2)

THIS PAGE INTENTIONALLY LEFT BLANK

DISTRIBUTION:

NAVAIRWARCENACDIV (4.3.3.5/Rusk), Bldg. 2187, Room 2340A (2)
48110 Shaw Point Road, Patuxent River, MD 20670-1906
Office of Naval Research (3.5.1) (1)
One Liberty Center, 875 N Randolph Street, Suite 1425
Arlington, VA 22203-1995
University of Dayton Research Institute (Pierce/Hoppe) (2)
Structural Integrity Division, 300 College Park, Dayton OH 45469-0120
Engineering Software Research and Development, Inc. (Lancaster/Actic/Szabo) (3)
111 West Port Plaza, Suite 825, St. Louis, MO 63146-3109
NAVAIRSYSCOM (AIR-5.1V), Bldg. 304, Room 106A (1)
22541 Millstone Road, Patuxent River, MD 20670-1606
NAVAIRSYSCOM (AIR-5.1), Bldg. 304, Room 100 (1)
22541 Millstone Road, Patuxent River, MD 20670-1606
NAVAIRWARCENACDIV (4.12.6.2), Bldg. 407, Room 116 (1)
22269 Cedar Point Road, Patuxent River, MD 20670-1120
NAVTESTWINGLANT (55TW01A), Bldg. 304, Room 200 (1)
22541 Millstone Road, Patuxent River, MD 20670-1606
DTIC (1)
Suite 0944, 8725 John J. Kingman Road, Ft. Belvoir, VA 22060-6218